nanomaterials

MDPI

Article

Facile Synthesis and Characterizations of Mixed Metal Oxide Nanoparticles for the Efficient Photocatalytic Degradation of Rhodamine B and Congo Red Dyes

Ehab A. Abdelrahman [1,2,*] and Eida S. Al-Farraj [1]

[1] Department of Chemistry, College of Science, Imam Mohammad Ibn Saud Islamic University (IMSIU), Riyadh 11623, Saudi Arabia
[2] Chemistry Department, Faculty of Science, Benha University, Benha 13518, Egypt
* Correspondence: eaaahmed@imamu.edu.sa or dr.ehabsaleh@yahoo.com

Abstract: Photocatalytic degradation has been suggested to be a cheap and efficient way to dispose of organic pollutants, such as dyes. Therefore, our research team strives to produce nanophotocatalysts in a simple and inexpensive way. In this work, the Pechini sol–gel technique was employed for the facile synthesis of $Mn_{0.5}Zn_{0.5}Fe_2O_4/Fe_2O_3$ and $Fe_{0.5}Mn_{0.5}Co_2O_4/Fe_2O_3$ as mixed metal oxide nanoparticles for the efficient photocatalytic degradation of Rhodamine B and Congo Red dyes. XRD, FT-IR, a N_2 adsorption/desorption analyzer, EDS, FE-SEM, and an UV–Vis diffuse reflectance spectrophotometer were used to characterize the produced samples. The XRD patterns revealed that the average crystallite size of the $Fe_{0.5}Mn_{0.5}Co_2O_4/Fe_2O_3$ and $Mn_{0.5}Zn_{0.5}Fe_2O_4/Fe_2O_3$ samples is 90.25 and 80.62 nm, respectively. The FE-SEM images revealed that the $Fe_{0.5}Mn_{0.5}Co_2O_4/Fe_2O_3$ sample consists of cubic and irregular shapes with an average diameter of 1.71 µm. Additionally, the $Mn_{0.5}Zn_{0.5}Fe_2O_4/Fe_2O_3$ sample consists of spherical shapes with an average diameter of 0.26 µm. The energy gaps of the $Fe_{0.5}Mn_{0.5}Co_2O_4/Fe_2O_3$ and $Mn_{0.5}Zn_{0.5}Fe_2O_4/Fe_2O_3$ samples are 3.50 and 4.3 eV and 3.52 and 4.20 eV, respectively. In the presence of hydrogen peroxide, the complete degradation of 100 mL of 20 mg/L of Rhodamine B and Congo Red dyes occurred at pH = 8 and 3, respectively, within 50 min, using 0.1 g of the synthesized samples.

Keywords: $Fe_{0.5}Mn_{0.5}Co_2O_4/Fe_2O_3$; $Mn_{0.5}Zn_{0.5}Fe_2O_4/Fe_2O_3$; Pechini sol–gel method; Rhodamine B dye; Congo Red; photocatalytic degradation

check for updates

Citation: Abdelrahman, E.A.; Al-Farraj, E.S. Facile Synthesis and Characterizations of Mixed Metal Oxide Nanoparticles for the Efficient Photocatalytic Degradation of Rhodamine B and Congo Red Dyes. *Nanomaterials* **2022**, *12*, 3992. https://doi.org/10.3390/nano12223992

Academic Editors: Stanisław Wacławek and Daniele Silvestri

Received: 24 October 2022
Accepted: 8 November 2022
Published: 12 November 2022

1. Introduction

Organic dyes are present in water sources due to their many industrial uses, such as in paper, textiles, food, cosmetics, and plastics. Because they can cause cancer and make cells change, these dye molecules are harmful to living things. Throwing liquid waste containing dyes into water leads to severe health risks for humans [1–5]. Therefore, effective strategies must be found to dispose of these pollutants.

Many methods are used to remove these pollutants, such as microfiltration, precipitation, reverse osmosis, chemical coagulation, photocatalytic degradation, and adsorption [6–15]. The recently arising solar-driven interfacial evaporation and photocatalysis method is a new strategy to remove organic pollutants from water with catalysts at the air–water interface [16–18].

Photocatalytic degradation has been suggested to be a cheap and efficient way to dispose of dye molecules. The absorption of photons by a photocatalyst results in the transmission of some electrons from the valence band to the conduction band. Hence, this simultaneously generates electrons and holes in the conduction and valence bands, respectively. Electrons and holes can produce hydroxyl free radicals when reacting with water. Organic dye pollutants can be quickly degraded by hydroxyl free radicals and converted into volatile gases, such as CO_2 and H_2O [19,20].

Congo Red and Rhodamine B dyes are utilized in numerous industries, such as the textile, chemical, pharmaceutical, paper, and cosmetic sectors. Consequently, a substantial quantity of these compounds contaminate water and enter normal water foundations. Due to the presence of aromatic amines in the composition of these compounds, ingestion of these dyes can cause cancer. This is why environmental rules require enterprises to remove these harmful compounds from polluted industrial fluids before releasing them into the environment [21–23].

There are many nanomaterials that are used as catalysts for the degradation of many organic dyes, such as $CuO/TiO_2/VO_2$, MgAlTi, ZnAlTi, perovskites, graphene oxide/silver nanocomposites, ZnO/montmorillonite nanocomposites, TiO_2-impregnated activated carbon, titanium oxo ethoxo clusters, nitrogen-doped TiO_2 nanotubes, and TiO_2/Fe_2O_3 nanocomposites [24–32]. Nanomaterials are characterized by a large surface area, high stability, and high efficiency in producing free radicals.

Several methods have been used to synthesize nanomaterials with a wide range of morphologies and sizes. The Pechini sol–gel method is widely used in the preparation of many nanomaterials, such as $CdTiO_3$, Y_2O_3, $SrTiO_3$, and $BaTiO_3$ [33–36]. However, most of the chemicals used to prepare these materials are very expensive. Therefore, our research team strives to produce nanophotocatalysts in a simple and inexpensive way.

Hence, in this work, the Pechini sol–gel technique was utilized for the facile synthesis of $Mn_{0.5}Zn_{0.5}Fe_2O_4/Fe_2O_3$ and $Fe_{0.5}Mn_{0.5}Co_2O_4/Fe_2O_3$ as mixed metal oxide nanoparticles for the efficient photocatalytic degradation of Rhodamine B and Congo Red dyes. The first innovative aspect of our research comes from the use of cheap salts, such as cobalt(II) chloride hexahydrate, iron(III) chloride hexahydrate, and manganese(II) acetate tetrahydrate to obtain these mixed nano-oxides for the first time. The other innovative aspect of our research comes from the ability of these nanomaterials to degrade a large concentration and a large volume of the Congo Red and Rhodamine B dyes in a short time. XRD, FT-IR, a N_2 adsorption/desorption analyzer, EDS, field-emission scanning electron microscopy, transmission electron microscopy, and an UV–Vis diffuse reflectance spectrophotometer were used to characterize the produced samples. In addition, the factors impacting the degradation of Rhodamine B and Congo Red dyes, such as pH, time, concentration, and catalyst quantity, were investigated.

2. Experimental Section

2.1. Chemicals

Ethylene glycol ($C_2H_6O_2$), cobalt(II) chloride hexahydrate ($CoCl_2.6H_2O$), hydrogen peroxide (H_2O_2), iron(III) chloride hexahydrate ($FeCl_3.6H_2O$), hydrochloric acid (HCl), manganese(II) acetate tetrahydrate ($Mn(CH_3COO)_2.4H_2O$), zinc(II) sulfate heptahydrate ($ZnSO_4.7H_2O$), sodium hydroxide (NaOH), Rhodamine B dye ($C_{28}H_{31}ClN_2O_3$), Congo Red dye ($C_{32}H_{22}N_6Na_2O_6S_2$), and tartaric acid ($C_4H_6O_6$) were purchased from Sigma Aldrich Company and used as received without further purification.

2.2. Synthesis of $Mn_{0.5}Zn_{0.5}Fe_2O_4/Fe_2O_3$ and $Fe_{0.5}Mn_{0.5}Co_2O_4/Fe_2O_3$ Samples

In 60 mL of distilled water, 8.33 g of $FeCl_3.6H_2O$, 4.43 g of $ZnSO_4.7H_2O$, 3.79 g of $Mn(CH_3COO)_2.4H_2O$, and 1.47 g of $CoCl_2.6H_2O$ were dissolved separately. Additionally, 13.25 g of tartaric acid was dissolved in 60 mL of distilled water. Fe(III), Zn(II), and Mn(II) solutions were mixed and stirred for 20 min to create the $Mn_{0.5}Zn_{0.5}Fe_2O_4/Fe_2O_3$ product. Moreover, Fe(III), Co(II), and Mn(II) solutions were mixed and stirred for 20 min to create the $Fe_{0.5}Mn_{0.5}Co_2O_4/Fe_2O_3$ product. Afterward, a tartaric acid solution was added to each system with continuous stirring for 20 min. Additionally, 3.33 mL of ethylene glycol was added to each system with continuous stirring. Furthermore, each system was heated at 150 °C until the solution was dried. Finally, the formed powder was ignited at 800 °C for 5 h. Scheme 1 summarizes the synthesizing steps of the nanomaterials.

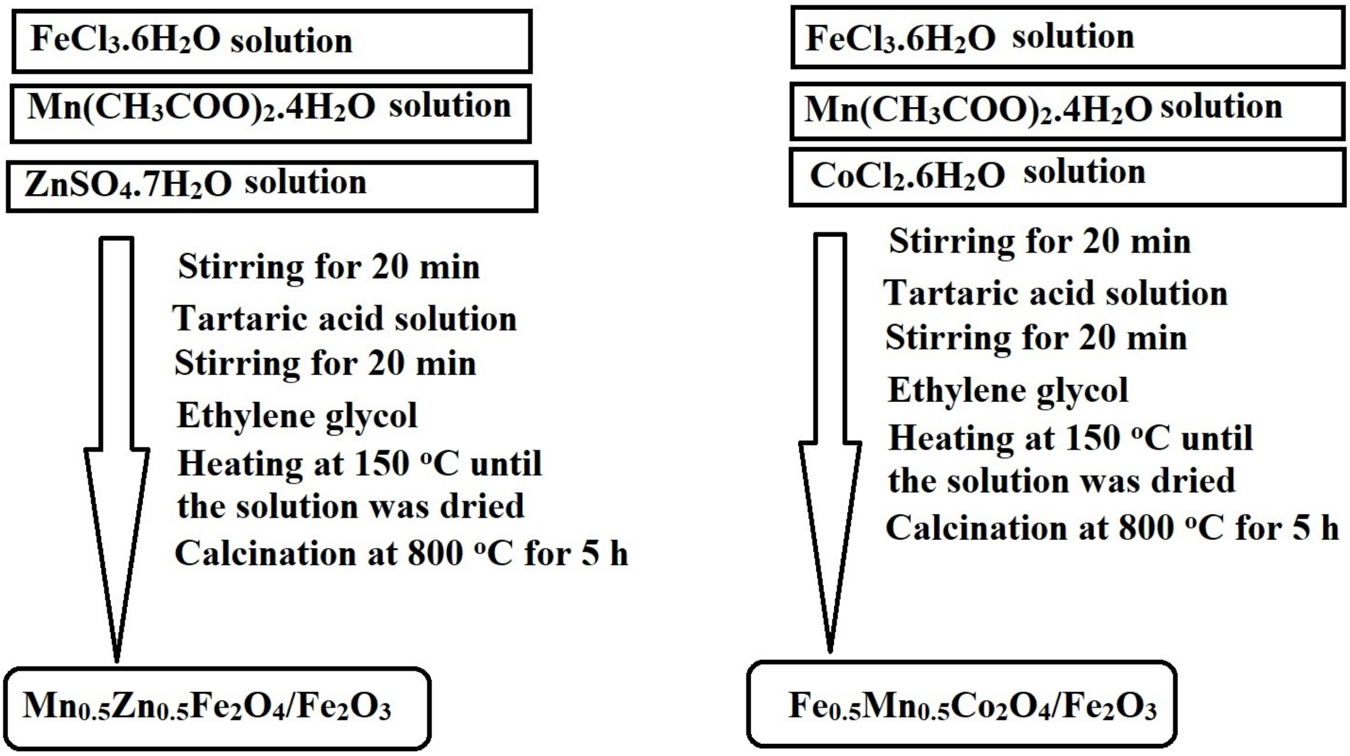

Scheme 1. The synthesizing steps of the nanomaterials.

2.3. Instrumentation

An X-ray diffraction (XRD) instrument was used to study the crystalline structure of the synthesized nanomaterials. The diffractograms were collected using a D8 Advance X-ray diffractometer equipped with K_{α}Cu radiation (λ = 0.15 nm). A Thermo Scientific Nicolet iS50 Fourier-transform infrared spectrometer (FT-IR) was used to study the functional groups of the synthesized nanomaterials. A Jasco V-750 UV–Vis diffuse reflectance spectrophotometer (DRS) and an integrating sphere, calibrated with barium sulfate, were used to determine the band gap of the synthesized nanomaterials. A Quantachrome NOVA Touch LX2 nitrogen-gas-sorption analyzer was used to study the surface textures (BET surface area, total pore volume, and average pore radius) of the synthesized nanomaterials. The synthesized nanomaterials were degassed at 110 °C for 24 h before analyses. A Quanta 250 FEG scanning electron microscope (SEM) attached with an energy dispersive X-ray unit was used to study the surface morphology and elemental analysis of the synthesized nanomaterials. The morphologies of the nanomaterials were obtained using a Talos F200iS transmission electron microscope (TEM). The concentration of Rhodamine B and Congo Red dyes was determined using a Jasco V-750 UV–Vis spectrophotometer. The maximum wavelengths of the Rhodamine B and Congo Red dyes were 554 and 497 nm, respectively.

2.4. Photocatalytic Degradation of Rhodamine B and Congo Red Dyes

For every experiment, a specified amount of the $Mn_{0.5}Zn_{0.5}Fe_2O_4/Fe_2O_3$ or $Fe_{0.5}Mn_{0.5}Co_2O_4/Fe_2O_3$ samples was dispersed in a 100 mL aqueous solution of Rhodamine B or Congo Red dyes. The suspension was then agitated magnetically in the dark for 60 min. The solution was then irradiated with three UV lamps (30 cm, 8 watt, and 225 nm) located 8 cm away from the dye solution. In addition, the nanomaterials were separated by centrifugation, and the remaining concentration of the Rhodamine B or Congo Red dyes in the filtrate was measured using a Jasco V-750 UV–Vis spectrophotometer. The same tests were conducted again, but this time 2 mL of 2 M hydrogen peroxide was added. The photodegradation efficiency (% D) of the nanomaterials against Rhodamine B or Congo Red dyes was determined using Equation (1).

$$\% \, D = \frac{X_d - X_e}{X_d} \times 100 \tag{1}$$

X_d (mg/L) is the remaining concentration of the Rhodamine B or Congo Red dyes after the process of stirring in the dark. X_e (mg/L) is the remaining concentration of the Rhodamine B or Congo Red dyes after exposure to ultraviolet rays.

3. Results and Discussion

3.1. Characterization of the Synthesized Nanocomposites

3.1.1. X-ray Diffraction

X-ray powder diffraction (XRD) is a rapid analytical technique primarily used for the phase identification of a crystalline material, and it can provide information on the average crystallite size. Figure 1A,B displays the X-ray diffraction patterns of the $Fe_{0.5}Mn_{0.5}Co_2O_4/Fe_2O_3$ and $Mn_{0.5}Zn_{0.5}Fe_2O_4/Fe_2O_3$ samples, respectively. The results reveal that the $Fe_{0.5}Mn_{0.5}Co_2O_4/Fe_2O_3$ sample consisted of hematite (Fe_2O_3) and cobalt manganese iron oxide ($Fe_{0.5}Mn_{0.5}Co_2O_4$), as indicated by JCPDS Nos. 00-024-0072 and 01-086-8898, respectively. Additionally, the $Mn_{0.5}Zn_{0.5}Fe_2O_4/Fe_2O_3$ sample consisted of hematite (Fe_2O_3) and manganese zinc iron oxide ($Mn_{0.5}Zn_{0.5}Fe_2O_4$), as indicated by JCPDS Nos. 00-024-0072 and 01-086-8880, respectively. The peaks of cobalt manganese iron oxide or manganese zinc iron oxide at 2θ = 74.17°, 62.66°, 57.16°, 53.85°, 43.38°, 37.06°, 35.45°, 30.10°, and 18.38° corresponded to lattice plans (533), (440), (511), (422), (400), (222), (311), (220), and (111), respectively, as obtained from JCPDS Nos. 01-086-8898 and 01-086-8880. The peaks of hematite at 2θ = 75.40°, 71.83°, 64.01°, 49.54°, 40.84°, 33.14°, and 24.07° corresponded to lattice plans (220), (1 0 10), (300), (024), (113), (104), and (012), respectively, as obtained from JCPDS No. 00-024-0072. The average crystallite size of the $Fe_{0.5}Mn_{0.5}Co_2O_4/Fe_2O_3$ and $Mn_{0.5}Zn_{0.5}Fe_2O_4/Fe_2O_3$ samples was 90.25 and 80.62 nm, respectively. This confirms the success of the Pechini sol–gel method in synthesizing new mixed nano-oxides. In this method, an aqueous solution of metal salts is mixed with tartaric acid. Chelation, or the formation of complex ring-shaped compounds around the metal cations, takes place in the solution. Ethylene glycol is then added, and the liquid is heated to 150 °C to allow the chelates to polymerize, or form large, cross-linked networks. As excess water is removed by heating, a solid polymeric resin is achieved. Eventually, at a higher temperature of 800 °C for 5 h, the resin is decomposed, and ultimately, mixed metal oxides are obtained. Hence, this explains the proportions of the elements in Table 1 [33].

Table 1. The weight percentages of the elements in the synthesized samples.

Elements	**Wt %**	
	$Fe_{0.5}Mn_{0.5}Co_2O_4/Fe_2O_3$	**$Mn_{0.5}Zn_{0.5}Fe_2O_4/Fe_2O_3$**
Fe	75.10	69.51
Mn	6.06	4.52
Co	8.24	—-
Zn	—-	10.29
O	10.60	15.68

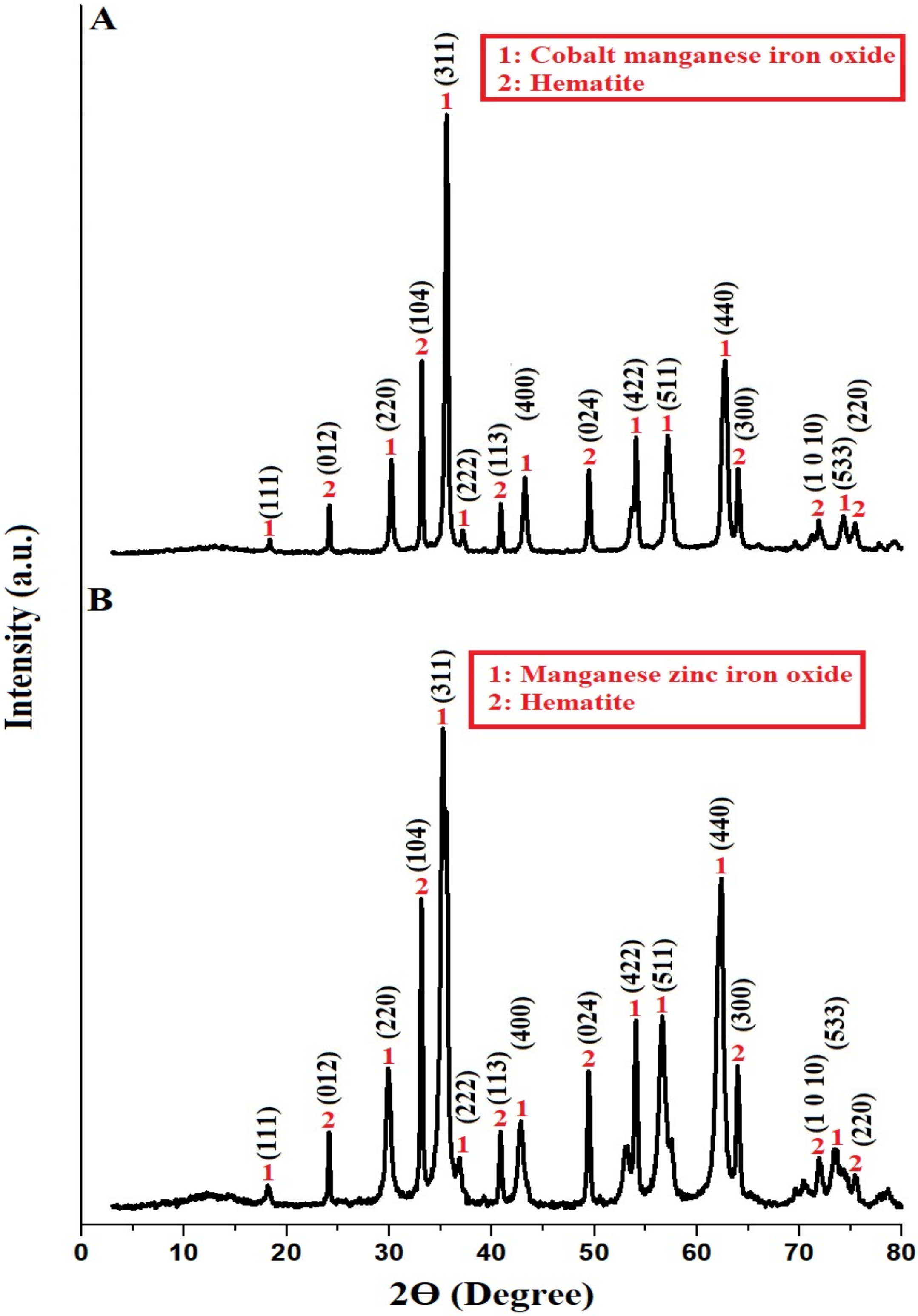

Figure 1. The X-ray diffraction patterns of the $Fe_{0.5}Mn_{0.5}Co_2O_4/Fe_2O_3$ (**A**) and $Mn_{0.5}Zn_{0.5}Fe_2O_4/Fe_2O_3$ (**B**) samples.

3.1.2. Energy Dispersive X-ray Spectroscopy

Energy dispersive X-ray spectroscopy (EDX) is an analytical method which yields a spectrum that displays the peaks correlated to the elemental composition of the investigated sample. Figure 2A,B displays the energy dispersive X-ray patterns of the

$Fe_{0.5}Mn_{0.5}Co_2O_4/Fe_2O_3$ and $Mn_{0.5}Zn_{0.5}Fe_2O_4/Fe_2O_3$ samples, respectively. The results reveal that the $Fe_{0.5}Mn_{0.5}Co_2O_4/Fe_2O_3$ sample consisted of manganese, oxygen, cobalt, and iron as displayed in Table 1. Additionally, the $Mn_{0.5}Zn_{0.5}Fe_2O_4/Fe_2O_3$ sample consisted of manganese, oxygen, zinc, and iron as displayed in Table 1. Hence, the absence of other elements confirms the success of the method in obtaining pure nano-oxides. The high percentage of iron in the $Fe_{0.5}Mn_{0.5}Co_2O_4/Fe_2O_3$ sample confirms the high percentage of Fe_2O_3 compared to $Fe_{0.5}Mn_{0.5}Co_2O_4$.

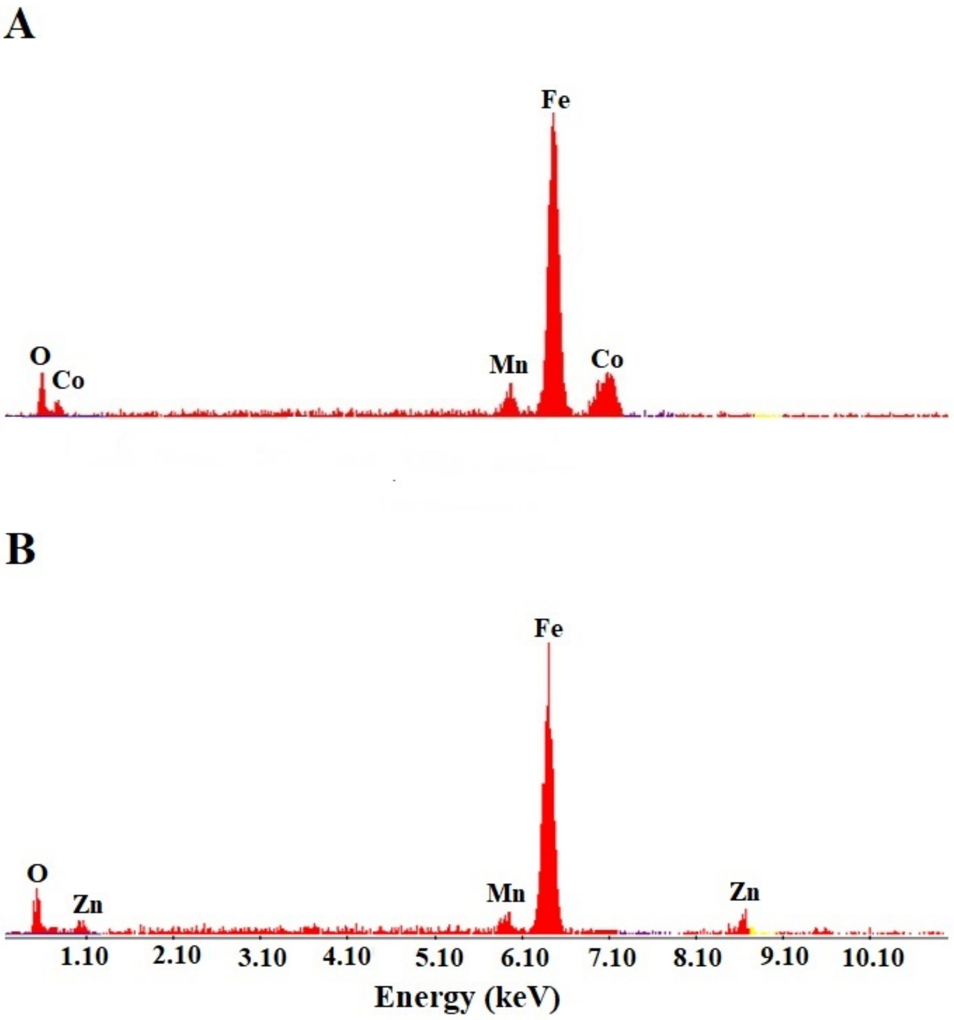

Figure 2. The energy dispersive X-ray patterns of the $Fe_{0.5}Mn_{0.5}Co_2O_4/Fe_2O_3$ (**A**) and $Mn_{0.5}Zn_{0.5}Fe_2O_4/Fe_2O_3$ (**B**) samples.

3.1.3. N_2 Adsorption/Desorption Analyzer

Figure 3A,B displays the plot of the volume adsorbed against the relative pressure of the $Fe_{0.5}Mn_{0.5}Co_2O_4/Fe_2O_3$ and $Mn_{0.5}Zn_{0.5}Fe_2O_4/Fe_2O_3$ samples, respectively. The results reveal that all curves belong to the IV types [37–39]. In addition, Table 2 displays the surface parameters, such as the BET surface area, total pore volume, and average pore size, of the produced samples. Moreover, the BET surface area of the $Mn_{0.5}Zn_{0.5}Fe_2O_4/Fe_2O_3$ sample is greater than that of the $Fe_{0.5}Mn_{0.5}Co_2O_4/Fe_2O_3$ sample. Hence, it was expected that the $Mn_{0.5}Zn_{0.5}Fe_2O_4/Fe_2O_3$ sample would outperform the $Fe_{0.5}Mn_{0.5}Co_2O_4/Fe_2O_3$ sample in the photocatalytic degradation efficiency of the dyes under study.

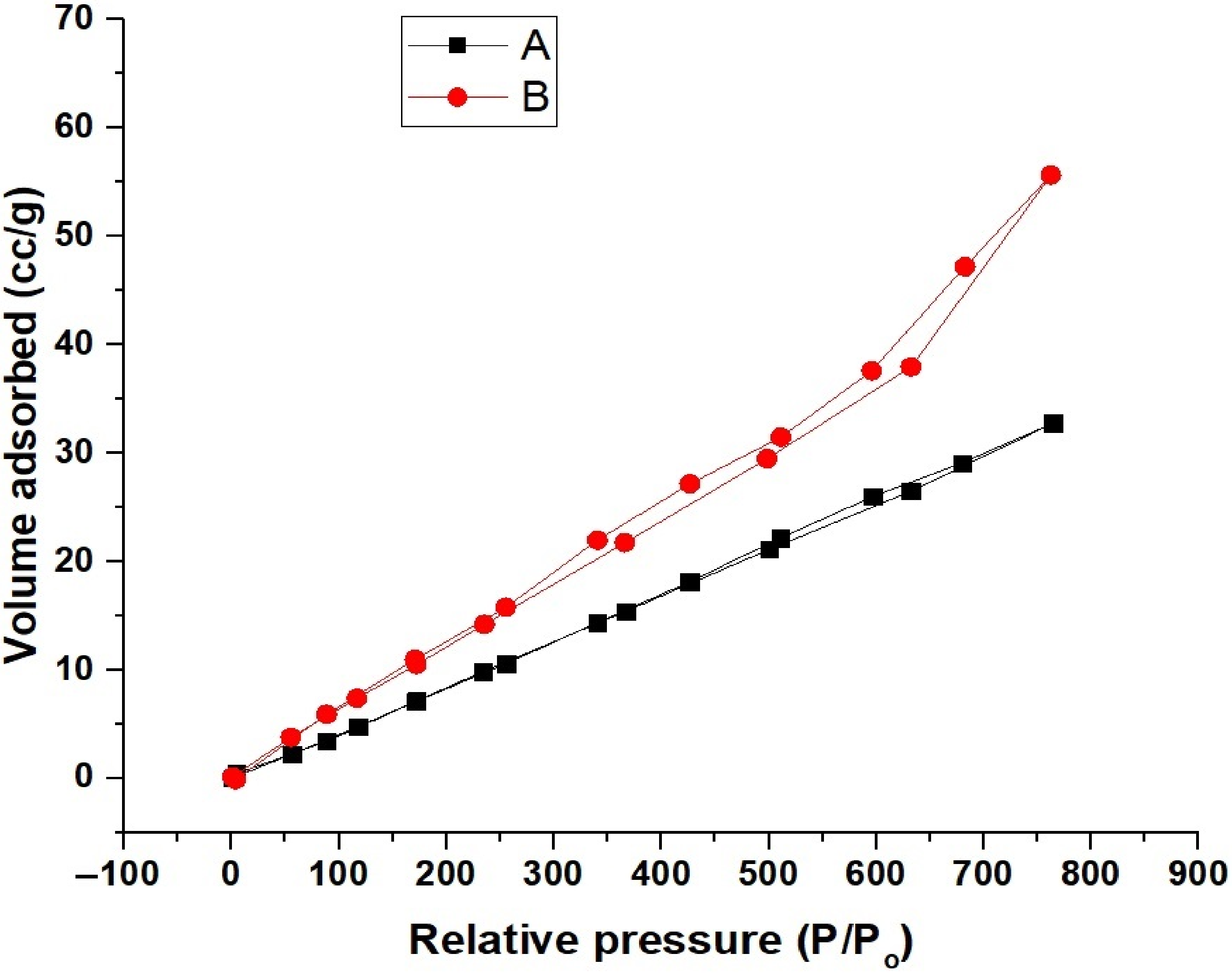

Figure 3. The plot of the volume adsorbed against the relative pressure for the $Fe_{0.5}Mn_{0.5}Co_2O_4/Fe_2O_3$ (A) and $Mn_{0.5}Zn_{0.5}Fe_2O_4/Fe_2O_3$ (B) samples.

Table 2. The BET surface area, total pore volume, and average pore size of the synthesized samples.

Surface Properties	**Sample**	
	$\mathbf{Mn_{0.5}Zn_{0.5}Fe_2O_4/Fe_2O_3}$	$\mathbf{Fe_{0.5}Mn_{0.5}Co_2O_4/Fe_2O_3}$
BET surface area (m^2/g)	62.7305	44.2141
Total pore volume (cc/g)	0.0490	0.0925
Average pore size (nm)	1.7235	3.2579

3.1.4. Field-Emission Scanning Electron Microscopy and Transmission Electron Microscopy

Figure 4A,B displays the scanning electron microscopy images of the $Fe_{0.5}Mn_{0.5}Co_2O_4/Fe_2O_3$ and $Mn_{0.5}Zn_{0.5}Fe_2O_4/Fe_2O_3$ samples, respectively. The results reveal that the surface of the $Fe_{0.5}Mn_{0.5}Co_2O_4/Fe_2O_3$ sample consisted of cubic and irregular shapes with an average grain size of 1.71 µm. Additionally, the surface of the $Mn_{0.5}Zn_{0.5}Fe_2O_4/Fe_2O_3$ sample consists of spherical shapes with an average grain size of 0.26 µm. XRD can determine the crystallite size, but SEM can determine the grain size, and the surface particles might consist of many aggregates of crystallites, which should be bigger than the crystallite size obtained from XRD.

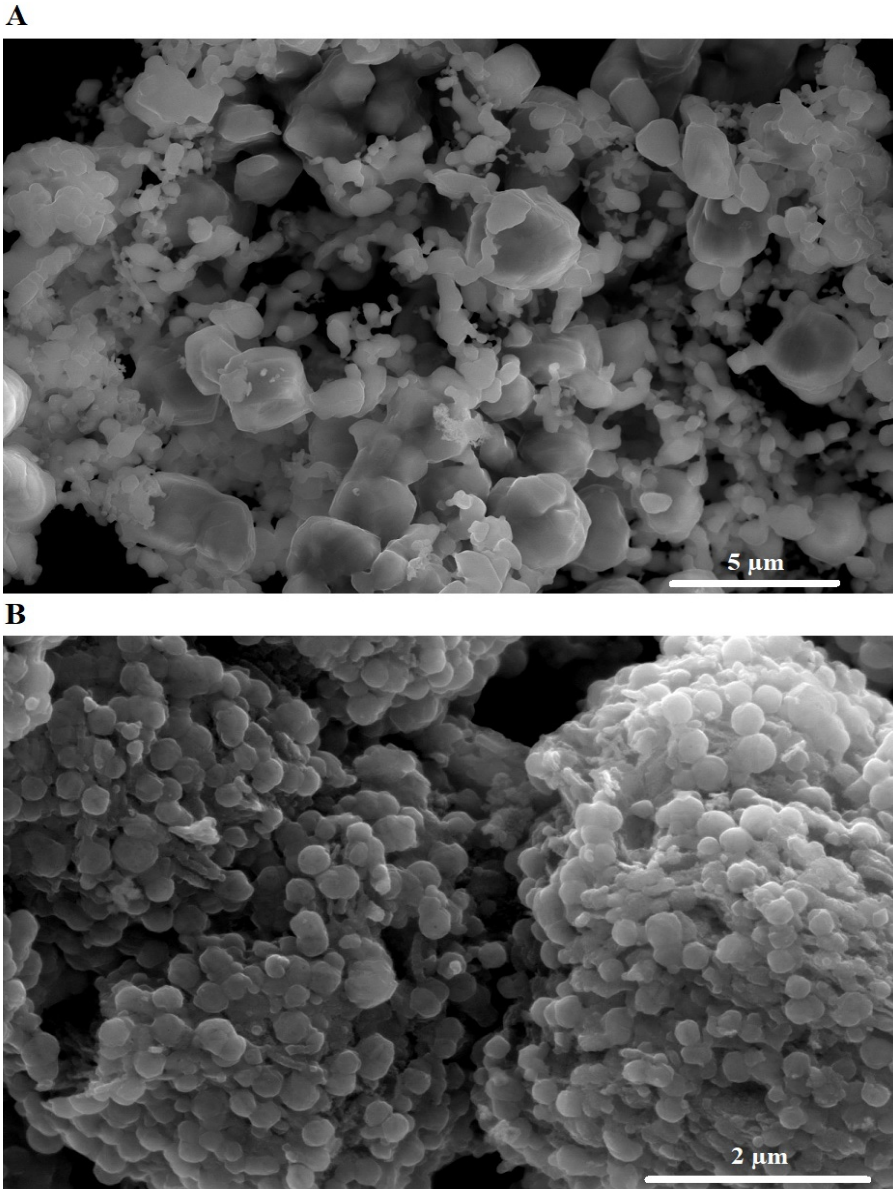

Figure 4. The scanning electron microscopy images of the $Fe_{0.5}Mn_{0.5}Co_2O_4/Fe_2O_3$ (**A**) and $Mn_{0.5}Zn_{0.5}Fe_2O_4/Fe_2O_3$ (**B**) samples.

Figure 5A,B displays the transmission electron microscopy images of the $Fe_{0.5}Mn_{0.5}Co_2O_4/Fe_2O_3$ and $Mn_{0.5}Zn_{0.5}Fe_2O_4/Fe_2O_3$ samples, respectively. The results reveal that the $Fe_{0.5}Mn_{0.5}Co_2O_4/Fe_2O_3$ and $Mn_{0.5}Zn_{0.5}Fe_2O_4/Fe_2O_3$ samples consisted of cubic and irregular shapes with an average diameter of 100.27 and 84.29 nm, respectively. The average particle size determined from the TEM images is slightly larger than that estimated from the XRD technique as a result of the presence of the agglomeration.

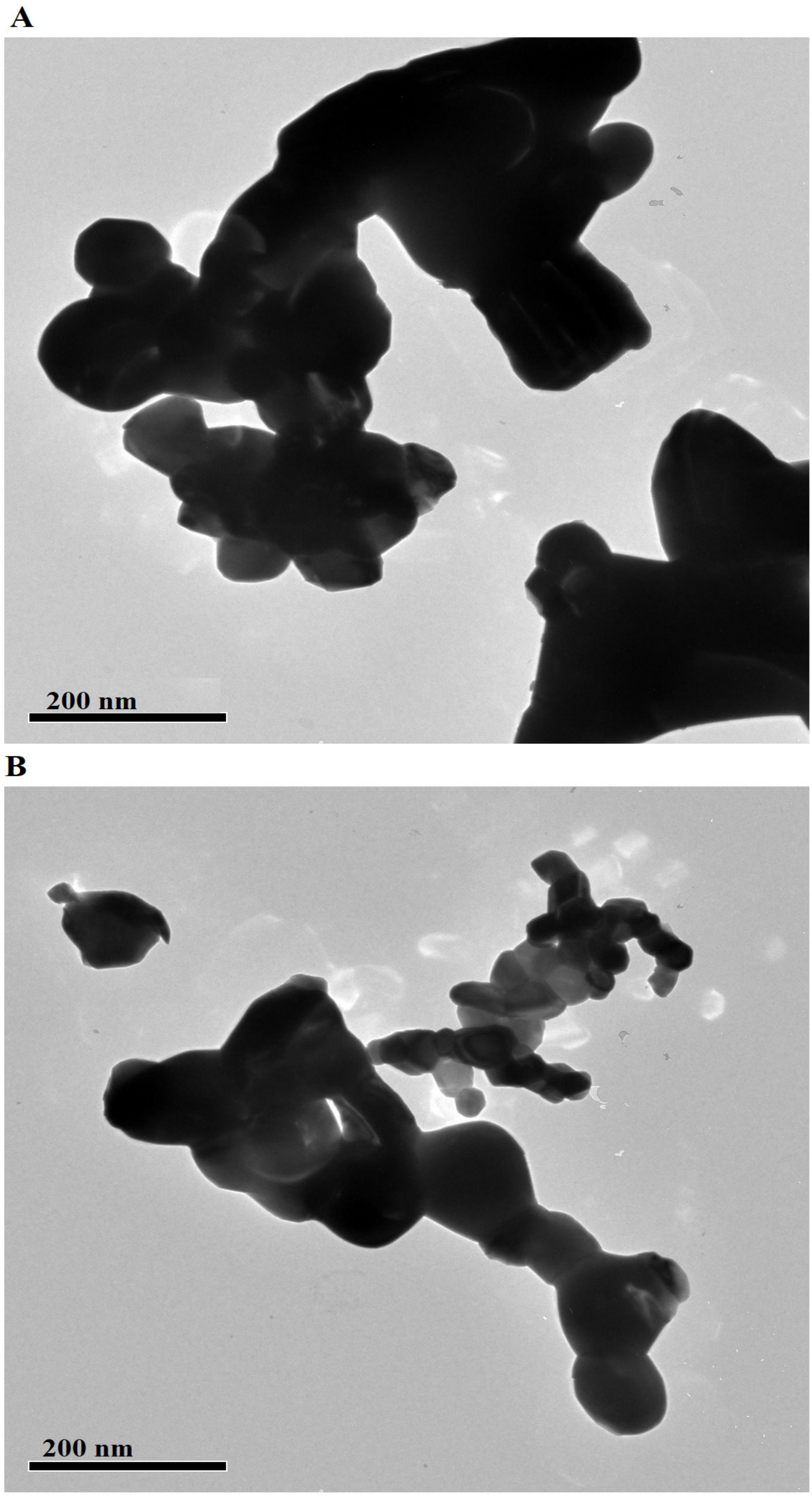

Figure 5. The transmission electron microscopy images of the $Fe_{0.5}Mn_{0.5}Co_2O_4/Fe_2O_3$ (**A**) and $Mn_{0.5}Zn_{0.5}Fe_2O_4/Fe_2O_3$ (**B**) samples.

3.1.5. FT-IR

Figure 6A,B displays the FT-IR spectra of the $Fe_{0.5}Mn_{0.5}Co_2O_4/Fe_2O_3$ and $Mn_{0.5}Zn_{0.5}Fe_2O_4/Fe_2O_3$ samples, respectively. The bands at 559 and 549 cm^{-1} in the $Fe_{0.5}Mn_{0.5}Co_2O_4/Fe_2O_3$ and $Mn_{0.5}Zn_{0.5}Fe_2O_4/Fe_2O_3$ samples were attributed to the bending vibrational modes of Fe-O, Mn-O, Co-O, and Zn-O in the $Fe_{0.5}Mn_{0.5}Co_2O_4$ and $Mn_{0.5}Zn_{0.5}Fe_2O_4/Fe_2O_3$ samples, respectively. The bands at 444 and 454 cm^{-1} in the $Fe_{0.5}Mn_{0.5}Co_2O_4/Fe_2O_3$ and $Mn_{0.5}Zn_{0.5}Fe_2O_4/Fe_2O_3$ samples were attributed to the bending vibrations of the Fe–O bond in the Fe_2O_3, respectively. The bands at 1625 and 1634 cm^{-1} in the $Fe_{0.5}Mn_{0.5}Co_2O_4/Fe_2O_3$ and $Mn_{0.5}Zn_{0.5}Fe_2O_4/Fe_2O_3$ samples, respectively, were attributed to the bending vibrations of the adsorbed water. The bands at 3433 and 3448 cm^{-1} in the $Fe_{0.5}Mn_{0.5}Co_2O_4/Fe_2O_3$ and $Mn_{0.5}Zn_{0.5}Fe_2O_4/Fe_2O_3$ nanocomposites, respectively, were attributed to the stretching vibrations of the adsorbed water [40].

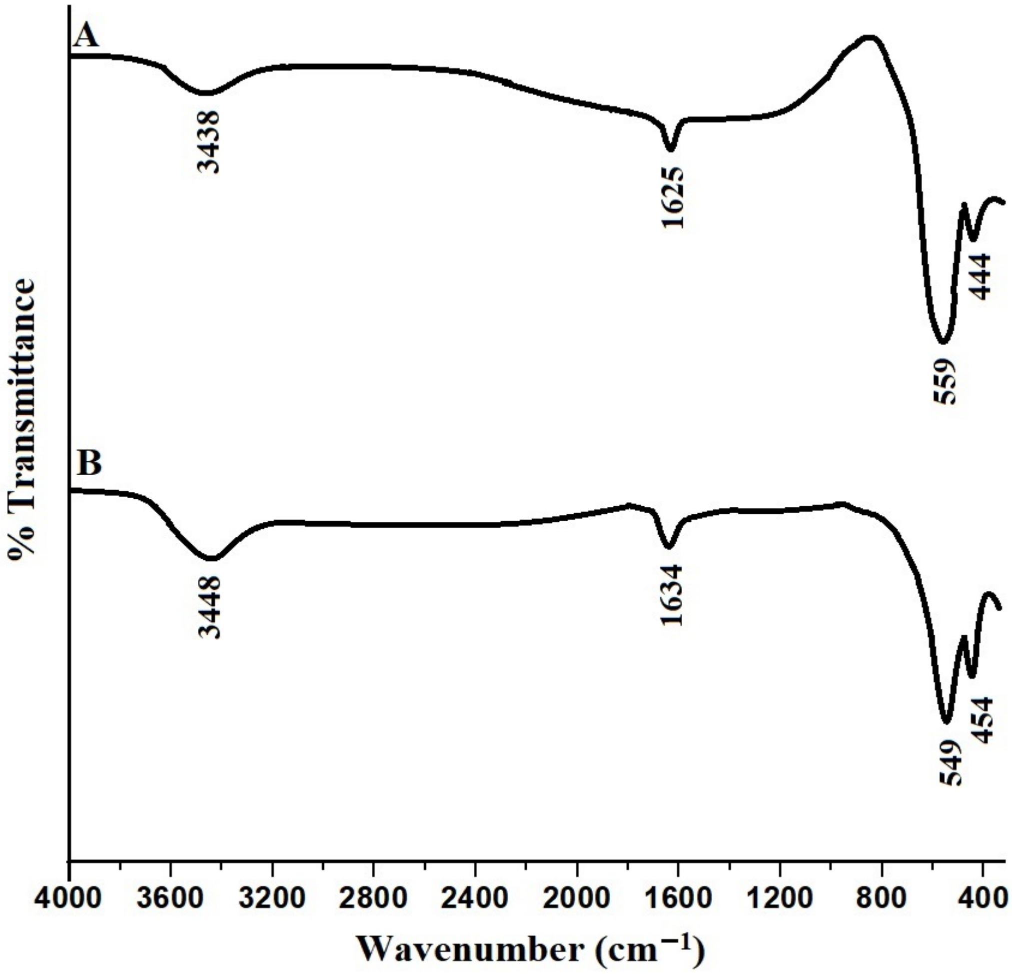

Figure 6. The FT-IR spectra of the $Fe_{0.5}Mn_{0.5}Co_2O_4/Fe_2O_3$ (**A**) and $Mn_{0.5}Zn_{0.5}Fe_2O_4/Fe_2O_3$ (**B**) samples.

3.1.6. Energy Gap

The energy gap (E_g) was determined using the diffuse reflectance spectra of the $Fe_{0.5}Mn_{0.5}Co_2O_4/Fe_2O_3$ and $Mn_{0.5}Zn_{0.5}Fe_2O_4/Fe_2O_3$ samples and Equation (2) [19].

$$(F(R)h\upsilon)^Z = K\,(h\upsilon - E_g) \tag{2}$$

F(R) is a constant, while K is the Kubelka–Munk function. Z is an integer based on the transition type. Z = 2 for the direct transitions that are permitted, while Z = 1/2 for the indirect transitions that are permitted. Figure 7A,B displays the plot of $(F(R)h\upsilon)^2$ against hυ for the $Fe_{0.5}Mn_{0.5}Co_2O_4/Fe_2O_3$ and $Mn_{0.5}Zn_{0.5}Fe_2O_4/Fe_2O_3$ samples, respectively. Therefore, the transitions that were most abundant in the synthesized nanocomposites were direct allowed transitions. The energy gap (E_g) is determined by extrapolating each graph until $(F(R)h\nu)^2$ equals 0. The energy gap of the $Fe_{0.5}Mn_{0.5}Co_2O_4/Fe_2O_3$ and $Mn_{0.5}Zn_{0.5}Fe_2O_4/Fe_2O_3$ samples was 3.50 and 4.3 eV and 3.52 and 4.20 eV, respectively.

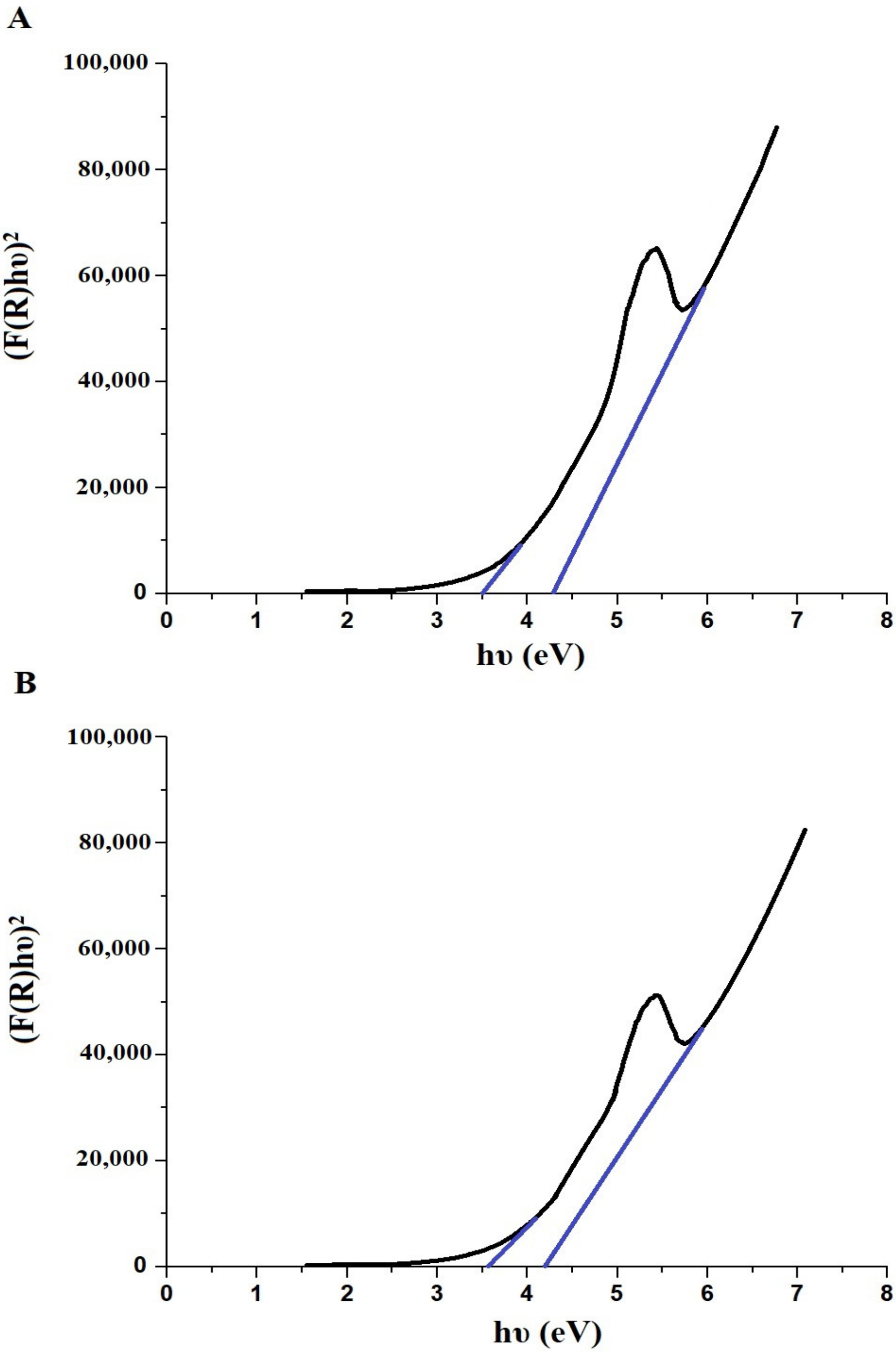

Figure 7. The plot of $(F(R)h\upsilon)^2$ against hυ for the $Fe_{0.5}Mn_{0.5}Co_2O_4/Fe_2O_3$ (**A**) and $Mn_{0.5}Zn_{0.5}Fe_2O_4/Fe_2O_3$ (**B**) samples.

3.2. Photocatalytic Degradation of Rhodamine B and Congo Red Dyes

3.2.1. Effect of pH

Figure 8A,B displays the plot of % D against pH for the degradation of Rhodamine B and Congo Red dyes using the $Fe_{0.5}Mn_{0.5}Co_2O_4/Fe_2O_3$ and $Mn_{0.5}Zn_{0.5}Fe_2O_4/Fe_2O_3$

samples, respectively. It is noticeable that by increasing the pH, the degradation efficiency of the synthesized samples toward Rhodamine B dye increased, while the degradation efficiency of the synthesized samples toward Congo Red dye decreased. Rhodamine B dye is a cationic dye whose adsorption is increased in alkaline media, and thus the efficiency of its degradation in alkaline media is increased [19]. Congo Red dye is an anionic dye whose adsorption is increased in acidic media, and thus the efficiency of its degradation in acidic media is increased [19]. In the case of using the $Fe_{0.5}Mn_{0.5}Co_2O_4/Fe_2O_3$ sample, the degradation efficiency of the sample toward Rhodamine B dye without H_2O_2 (pH = 8), Rhodamine B dye with H_2O_2 (pH = 8), Congo Red dye without H_2O_2 (pH = 3), and Congo Red dye with H_2O_2 (pH = 3) was equal to 46.02, 100, 36.11, and 100 %, respectively. In the case of using the $Mn_{0.5}Zn_{0.5}Fe_2O_4/Fe_2O_3$ sample, the degradation efficiency of the sample toward Rhodamine B dye without H_2O_2 (pH = 8), Rhodamine B dye with H_2O_2 (pH = 8), Congo Red dye without H_2O_2 (pH = 3), and Congo Red dye with H_2O_2 (pH = 3) was equal to 47.14, 100, 47.53, and 100 %, respectively.

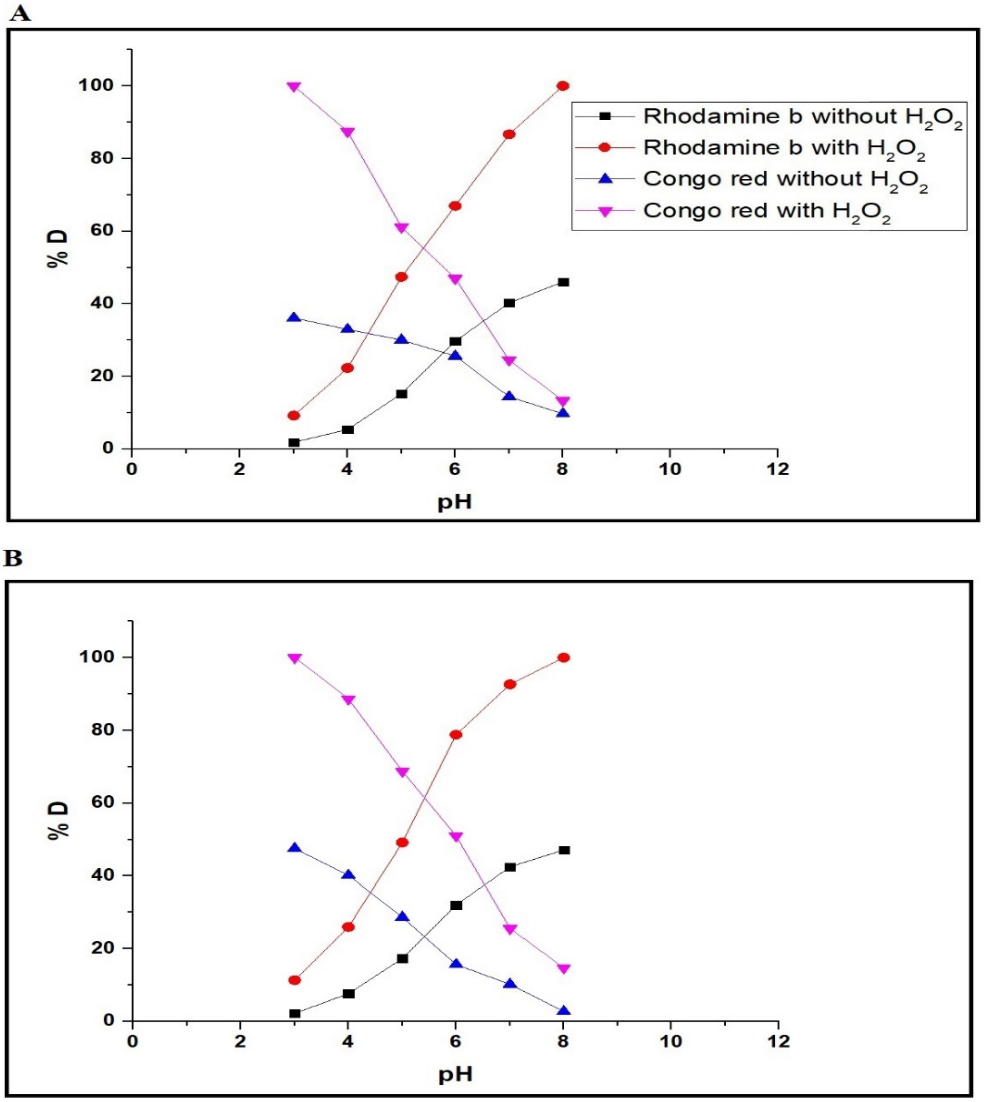

Figure 8. The plot of % D against pH for the degradation of Rhodamine B and Congo Red dyes using the $Fe_{0.5}Mn_{0.5}Co_2O_4/Fe_2O_3$ (**A**) and $Mn_{0.5}Zn_{0.5}Fe_2O_4/Fe_2O_3$ (**B**) samples. Experimental parameters: Concentration of dye = 20 mg/L; Volume of dye = 100 mL; Quantity of catalyst = 0.1 g; UV irradiation time = 100 min.

3.2.2. Effect of Time

Figure 9A,B displays the plot of % D against time for the degradation of Rhodamine B and Congo Red dyes using the $Fe_{0.5}Mn_{0.5}Co_2O_4/Fe_2O_3$ and $Mn_{0.5}Zn_{0.5}Fe_2O_4/Fe_2O_3$ samples, respectively. In the absence of hydrogen peroxide, it was observed that by increasing the time from 10 to 80 min, the degradation efficiency of the synthesized samples toward Rhodamine B and Congo Red dyes increased. Additionally, in the case of increasing the time from 80 to 120 min, there was no significant change in the degradation efficiency of the synthesized samples toward Rhodamine B and Congo Red dyes due to the saturation of the active sites of the samples [19]. In the presence of hydrogen peroxide, the complete degradation of Rhodamine B and Congo Red dyes occurred within 50 min. The Rhodamine B and Congo Red dyes were completely degraded under UV light using only hydrogen peroxide in the absence of the synthesized samples within 5 h, which is much larger than the consumed time (50 min) in the presence of the synthesized samples.

The degradation of Rhodamine B and Congo Red dyes using the synthesized samples is compatible with the first-order kinetic model as indicated by Equation (3) [19].

$$\ln\,(X_d/X_e) = k\,t \tag{3}$$

k (1/min) represents the first-order constant. Figure 10A,B displays the plot of ln (X_d/X_e) against t for the degradation of the Rhodamine B and Congo Red dyes using the $Fe_{0.5}Mn_{0.5}Co_2O_4/Fe_2O_3$ and $Mn_{0.5}Zn_{0.5}Fe_2O_4/Fe_2O_3$ samples, respectively. Tables 3 and 4 display the values for k and R^2 in the case of using the $Fe_{0.5}Mn_{0.5}Co_2O_4/Fe_2O_3$ and $Mn_{0.5}Zn_{0.5}Fe_2O_4/Fe_2O_3$ samples, respectively. Hydrogen peroxide increases the efficiency of dye degradation, and thus the k value increases when using hydrogen peroxide compared to when it is absent.

Table 3. The k and R^2 values for the degradation of Rhodamine B and Congo Red dyes using the $Fe_{0.5}Mn_{0.5}Co_2O_4/Fe_2O_3$ sample.

Dye	**k (1/min)**		**R^2**	
	With H_2O_2	**Without H_2O_2**	**With H_2O_2**	**Without H_2O_2**
Rhodamine B dye	0.0076	0.0414	0.9139	0.9993
Congo Red dye	0.0061	0.0342	0.9479	0.9939

Table 4. The k and R^2 values for the degradation of Rhodamine B and Congo Red dyes using the $Mn_{0.5}Zn_{0.5}Fe_2O_4/Fe_2O_3$ sample.

Dye	**k (1/min)**		**R^2**	
	With H_2O_2	**Without H_2O_2**	**With H_2O_2**	**Without H_2O_2**
Rhodamine B dye	0.0081	0.0475	0.0057	0.0303
Congo Red dye	0.9318	0.9695	0.9696	0.9965

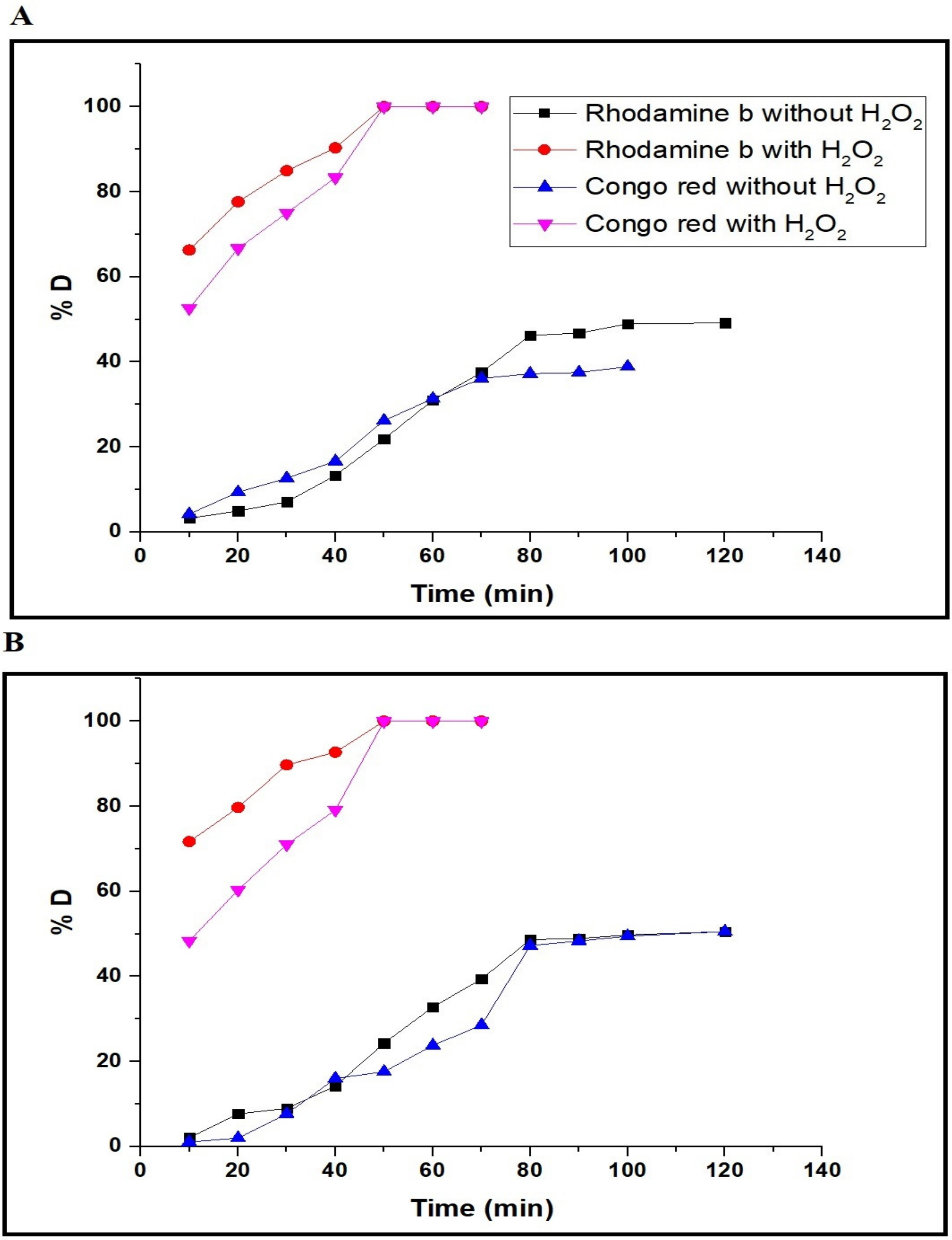

Figure 9. The plot of % D against time for the degradation of Rhodamine B and Congo Red dyes using the $Fe_{0.5}Mn_{0.5}Co_2O_4/Fe_2O_3$ (**A**) and $Mn_{0.5}Zn_{0.5}Fe_2O_4/Fe_2O_3$ (**B**) samples. Experimental parameters: Concentration of dye = 20 mg/L; Volume of dye = 100 mL; Quantity of catalyst = 0.1 g; pH = 8 and 3 in the case of Rhodamine B and Congo Red dyes, respectively.

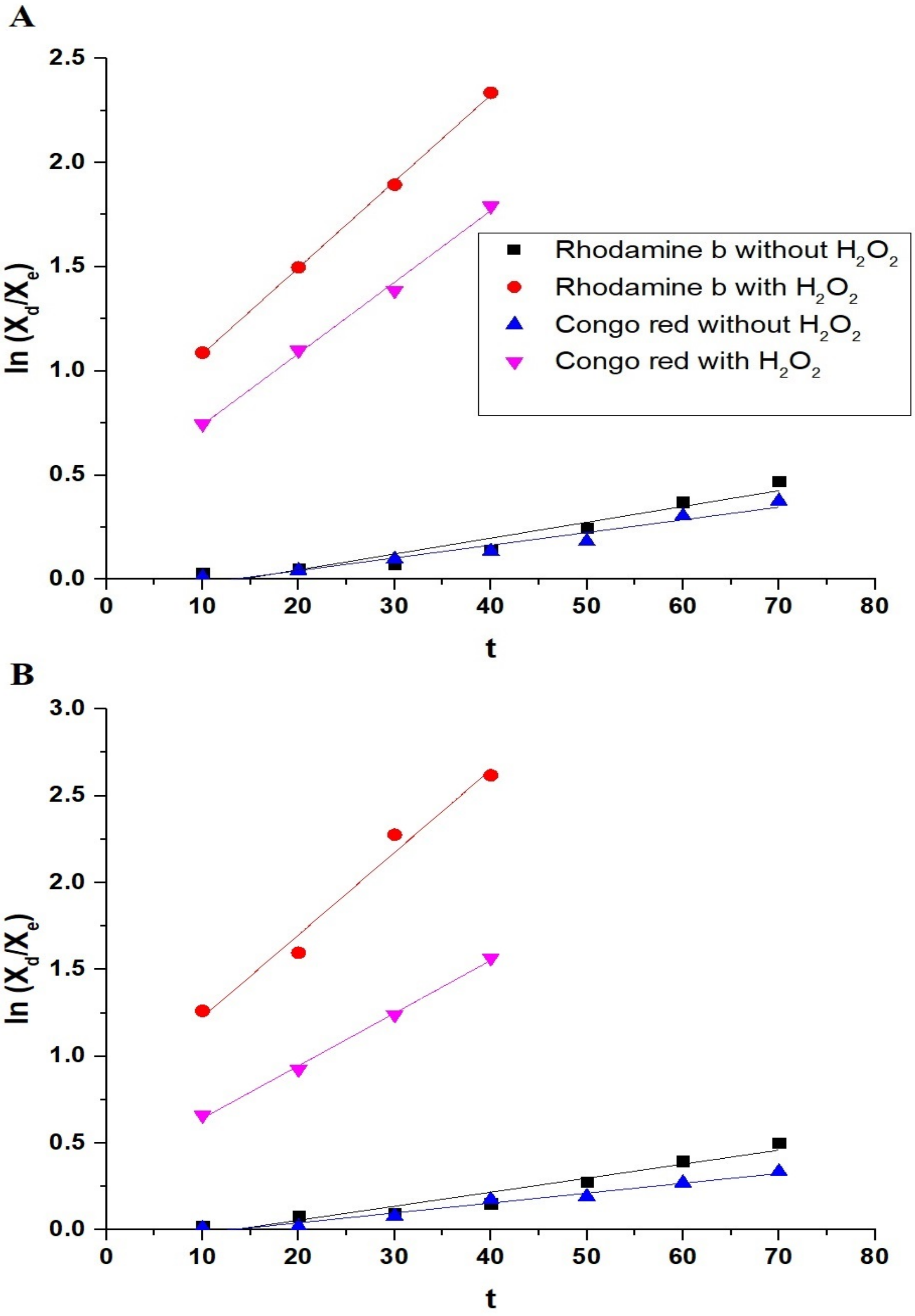

Figure 10. The plot of ln (X_d/X_e) against t for the degradation of Rhodamine B and Congo Red dyes using the $Fe_{0.5}Mn_{0.5}Co_2O_4/Fe_2O_3$ (**A**) and $Mn_{0.5}Zn_{0.5}Fe_2O_4/Fe_2O_3$ (**B**) samples.

3.2.3. Effect of Quantity of Catalyst

Figure 11A,B displays the plot of % D against the quantity of the $Fe_{0.5}Mn_{0.5}Co_2O_4/Fe_2O_3$ and $Mn_{0.5}Zn_{0.5}Fe_2O_4/Fe_2O_3$ samples for the degradation of the Rhodamine B and Congo

Red dyes, respectively. It has been observed that by increasing the quantity of samples from 0.025 to 0.1 g, the degradation efficiency of the synthesized samples toward Rhodamine B and Congo Red dyes increases because of the increase in active sites [19]. Additionally, when the quantity of the samples was increased from 0.1 to 0.2 g, there was a significant decrease in the degradation efficiency of the synthesized samples toward Rhodamine B and Congo Red dyes because of the turbidity caused by the particles of the catalyst, which impedes the arrival of light to it [19].

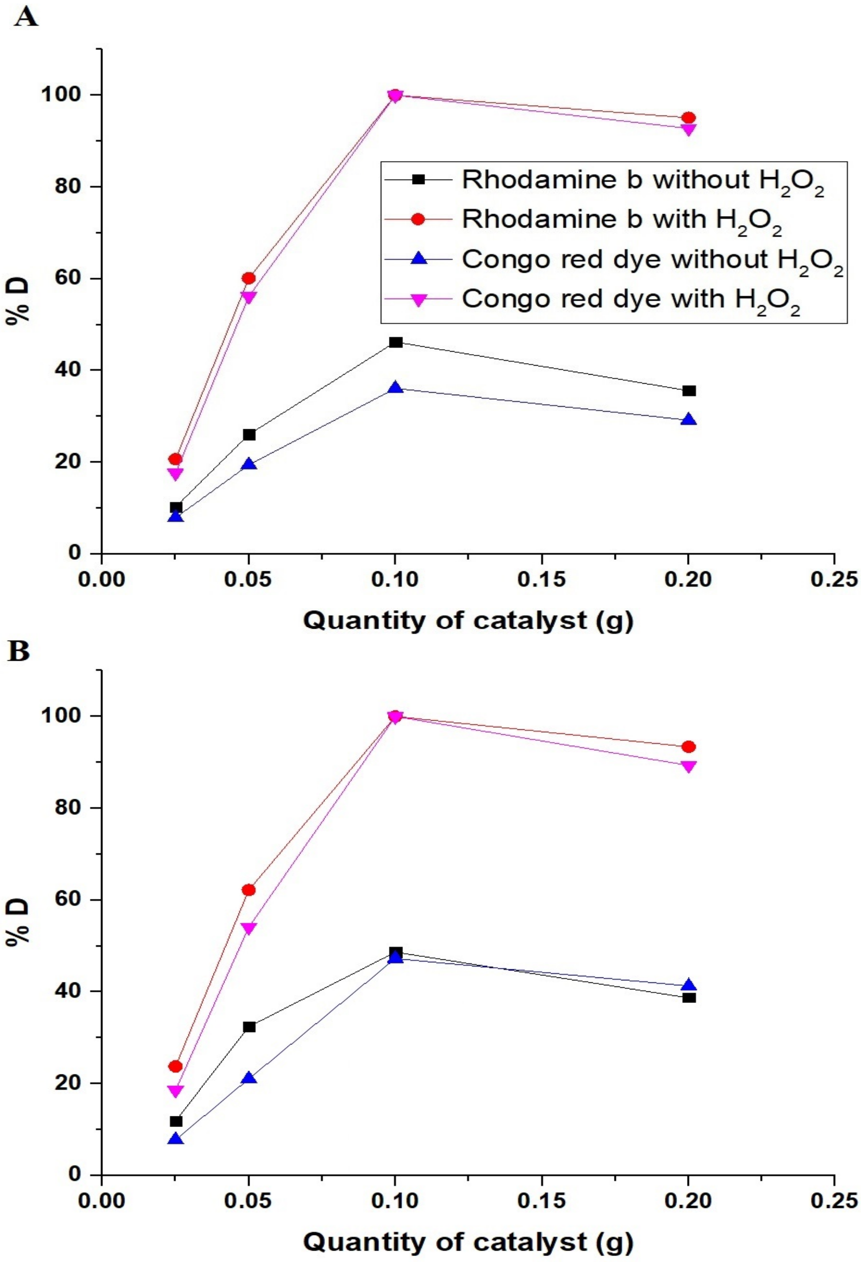

Figure 11. The plot of % D against the quantity of the $Fe_{0.5}Mn_{0.5}Co_2O_4/Fe_2O_3$ (**A**) and $Mn_{0.5}Zn_{0.5}Fe_2O_4/Fe_2O_3$ (**B**) samples for the degradation of Rhodamine B and Congo Red dyes. Experimental parameters: Concentration of dye = 20 mg/L; Volume of dye = 100 mL; pH = 8 and 3 in the case of Rhodamine B and Congo Red dyes, respectively. Time = 80 and 50 min in the absence and presence of H_2O_2, respectively.

3.2.4. Effect of Concentration

Figure 12A,B displays the plot of the % D of the Rhodamine B and Congo Red dyes against the concentration of the dyes, using the $Fe_{0.5}Mn_{0.5}Co_2O_4/Fe_2O_3$ and $Mn_{0.5}Zn_{0.5}Fe_2O_4/Fe_2O_3$ samples, respectively. It has been observed that by increasing the concentration of the Rhodamine B and Congo Red dyes from 10 to 30 mg/L, the degradation efficiency of the synthesized nanocomposites toward the Rhodamine B and Congo Red dyes decreases because the high concentration makes the dye particles block light from reaching the samples [19].

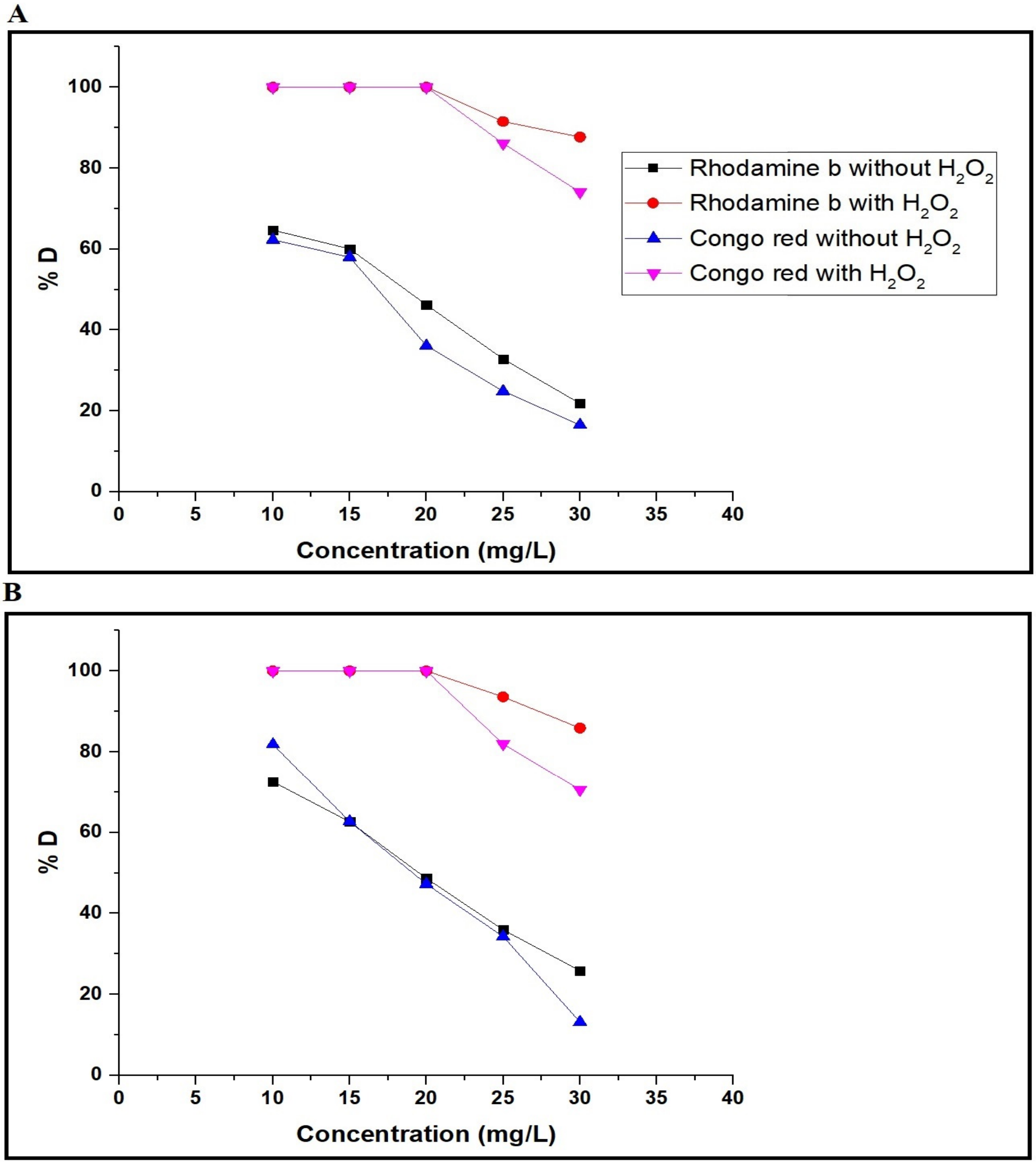

Figure 12. The plot of % D against the concentration of Rhodamine B and Congo Red dyes using the $Fe_{0.5}Mn_{0.5}Co_2O_4/Fe_2O_3$ (**A**) and $Mn_{0.5}Zn_{0.5}Fe_2O_4/Fe_2O_3$ (**B**) samples. Experimental parameters: Volume of dye = 100 mL; Quantity of catalyst = 0.1 g; pH = 8 and 3 in the case of Rhodamine B and Congo Red dyes, respectively. Time = 80 and 50 min in the absence and presence of H_2O_2, respectively.

3.2.5. Effect of Reusability

Figure 13A,B displays the plot of % D against the cycle number for the degradation of the Rhodamine B and Congo Red dyes using the $Fe_{0.5}Mn_{0.5}Co_2O_4/Fe_2O_3$ and $Mn_{0.5}Zn_{0.5}Fe_2O_4/Fe_2O_3$ samples, respectively. The results demonstrate a minor variation in the value of % D after four cycles, confirming the efficacy of the synthesized samples and their reusability with nearly the same efficiency in degrading the Rhodamine B and Congo Red dyes.

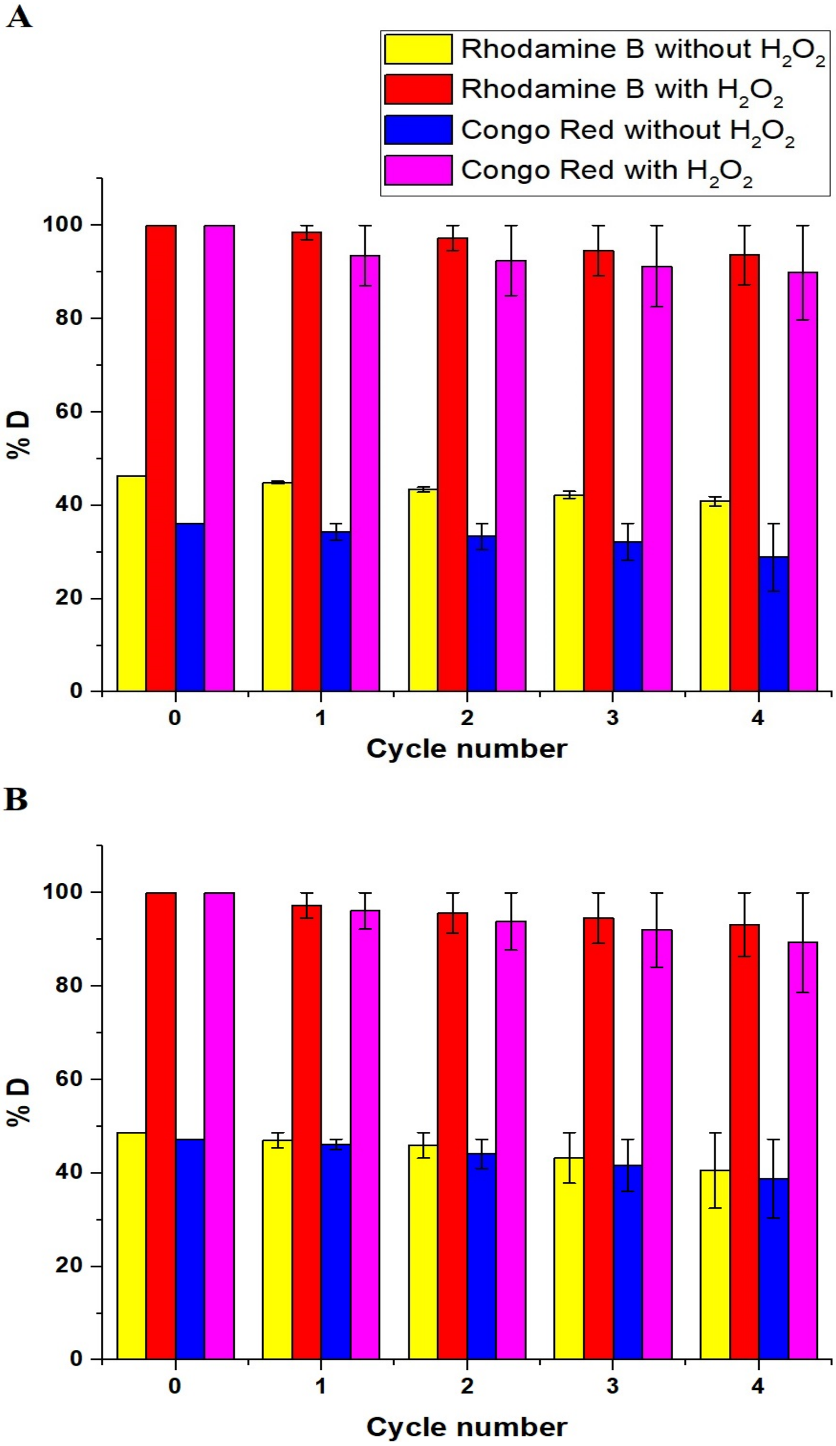

Figure 13. The plot of % D against cycle number for the degradation of Rhodamine B and Congo Red dyes using the $Fe_{0.5}Mn_{0.5}Co_2O_4/Fe_2O_3$ (**A**) and $Mn_{0.5}Zn_{0.5}Fe_2O_4/Fe_2O_3$ (**B**) samples.

3.3. Mechanism of Photocatalytic Degradation

Figure 14 displays the suggested mechanism for the degradation of Rhodamine B and Congo Red dyes using the $Fe_{0.5}Mn_{0.5}Co_2O_4/Fe_2O_3$ and $Mn_{0.5}Zn_{0.5}Fe_2O_4/Fe_2O_3$ samples. The absorption of photons by a photocatalyst results in the transmission of some electrons from the valence band to the conduction band. Hence, this simultaneously generates electrons and holes in the conduction and valence bands, respectively. Electrons and holes can produce hydroxyl free radicals when reacting with water. Rhodamine B and Congo Red dyes can be quickly degraded by hydroxyl free radicals and converted into volatile gases, such as CO_2 and H_2O [19,20].

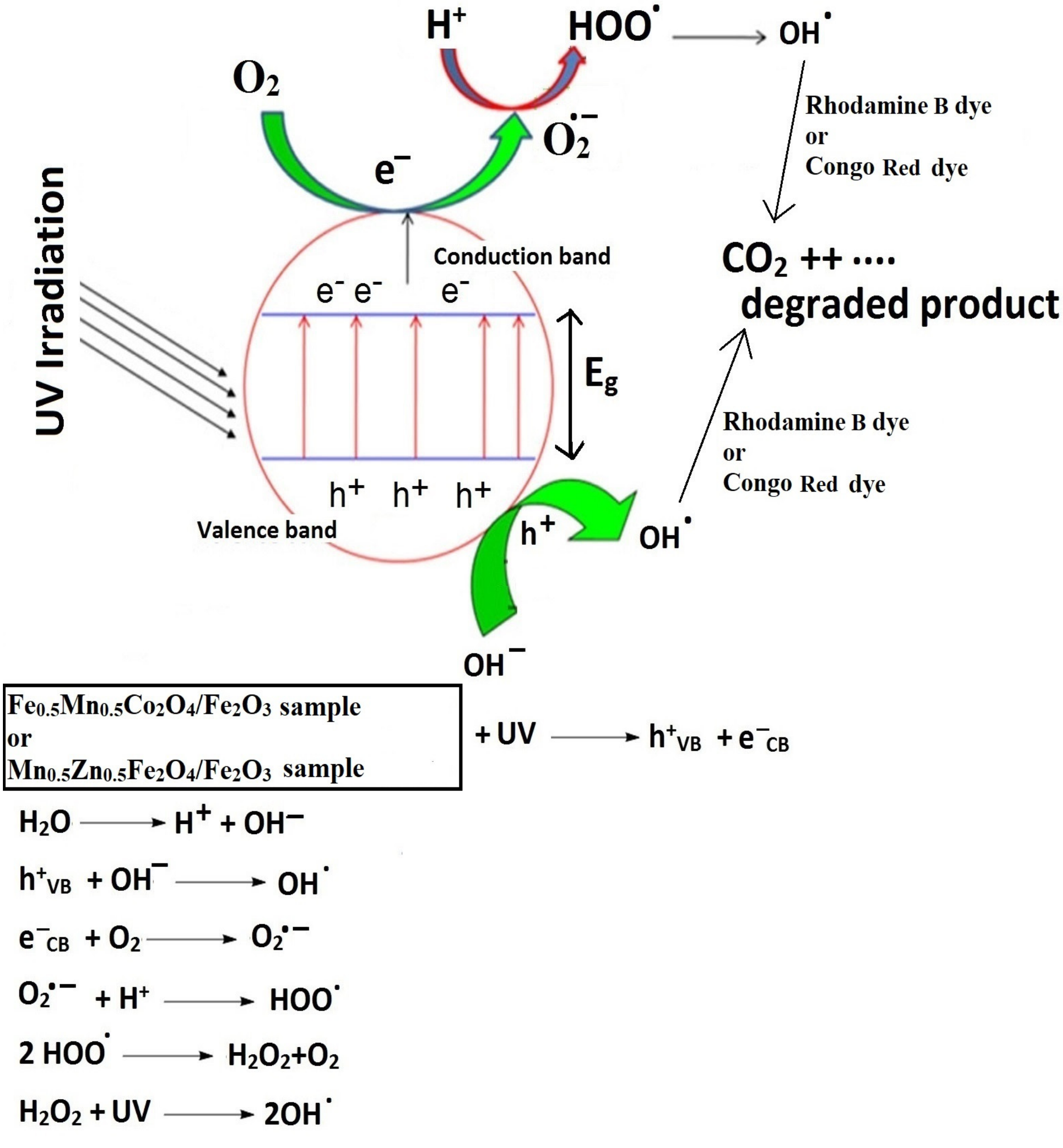

Figure 14. The suggested mechanism for the degradation of Rhodamine B and Congo Red dyes using the $Fe_{0.5}Mn_{0.5}Co_2O_4/Fe_2O_3$ and $Mn_{0.5}Zn_{0.5}Fe_2O_4/Fe_2O_3$ samples.

3.4. A Comparison between the Synthesized Nanocomposites and other Catalysts in the Literature for the Degradation of Rhodamine B and Congo Red Dyes

The % D of the Rhodamine B dye utilizing the $Fe_{0.5}Mn_{0.5}Co_2O_4/Fe_2O_3$ and $Mn_{0.5}Zn_{0.5}Fe_2O_4/Fe_2O_3$ samples was compared to that of other catalysts used in earlier studies, including the ZnO/SnO_2 composite, Fe/SnO_2 composite, $Fe_3O_4/TiO_2/CoMoO_4$ composite, Fe_3O_4/TiO_2 composite, chitosan/SnO_2 composite, $Fe_3O_4/SiO_2/TiO_2$ composite, BiOI/BiOCl composite, and ZnO/$PbCrO_4$ composite as displayed in Table 5 [41–48]. The % D of the Congo Red dye utilizing the $Fe_{0.5}Mn_{0.5}Co_2O_4/Fe_2O_3$ and $Mn_{0.5}Zn_{0.5}Fe_2O_4/Fe_2O_3$ samples was compared to that of other catalysts used in earlier studies, including the $ZrO_2/CeO_2/ZnO$, Au/ZnO, Ag/ZnO, magnetic silica-coated Ag_2WO_4/Ag_2S, and TiO_2-doped cobalt ferrite as displayed in Table 6 [49–52]. The results demonstrate the photocatalytic superiority of the $Fe_{0.5}Mn_{0.5}Co_2O_4/Fe_2O_3$ and $Mn_{0.5}Zn_{0.5}Fe_2O_4/Fe_2O_3$ samples over other photocatalysts used in previous studies because they degrade a large volume of a high concentration of Rhodamine B and Congo Red dyes in a short period of time with high efficiency. Thus, these synthesized catalysts are joined to a series of active materials for the degradation of organic materials [53,54]. Feng et al. utilized a new dual-mode-driven micromotor based on foam-like carbon nitride (f-C_3N_4) with precipitated Fe_3O_4 nanoparticles, namely Fe_3O_4/f-C_3N_4, powered by chemical/magnetic stimuli for a rapid reduction in organic pollutants [55]. Li et al. prepared an ordered Schottky heterojunction of heptazine-based crystalline carbon nitride (HCN) and Ti_3C_2 MXene through the ionothermal method. The HCN/Ti_3C_2 composites exhibit higher photocatalytic performance than pristine HCN [56].

Table 5. Comparison between the photocatalytic activities of the $Fe_{0.5}Mn_{0.5}Co_2O_4/Fe_2O_3$ and $Mn_{0.5}Zn_{0.5}Fe_2O_4/Fe_2O_3$ samples and those of other catalysts in earlier studies toward the Rhodamine B dye.

Catalyst	Concentration of Dye (mg/L)	Volume of Dye (mL)	Amount of Catalyst (g)	% D	Time (min)	Ref
BiOI/BiOCl composite	5	50	0.025	99.2	60	[41]
ZnO/$PbCrO_4$ composite	4.79	100	0.1	95	60	[42]
Chitosan/SnO_2 composite	4.79	100	0.05	95	60	[43]
$Fe_3O_4/SiO_2/TiO_2$ composite	30	50	0.05	29.5	60	[44]
$Fe_3O_4/TiO_2/CoMoO_4$ composite	20	50	0.05	98.7	17	[45]
Fe_3O_4/TiO_2 composite	10	100	0.05	91	120	[46]
ZnO/SnO_2 composite	0.958	50	0.05	80	120	[47]
Fe/SnO_2 composite	10	50	0.025	55	120	[48]
$Fe_{0.5}Mn_{0.5}Co_2O_4/Fe_2O_3$ composite	20	100	0.1	100	50	This study
$Mn_{0.5}Zn_{0.5}Fe_2O_4/Fe_2O_3$ nanocomposite	20	100	0.1	100	50	This study

Table 6. Comparison between the photocatalytic activities of the $Fe_{0.5}Mn_{0.5}Co_2O_4/Fe_2O_3$ and $Mn_{0.5}Zn_{0.5}Fe_2O_4/Fe_2O_3$ samples and those of other catalysts in earlier studies toward the Congo Red dye.

Catalyst	Concentration of Dye (mg/L)	Volume of Dye (mL)	Amount of Catalyst (g)	% D	Time (min)	Ref
$ZrO_2/CeO_2/ZnO$	10	100	0.005	86	250	[49]
Au/ZnO	16	100	0.05	77.2	150	[50]
Ag/ZnO	16	100	0.05	81.6	150	[50]
Magnetic silica-coated Ag_2WO_4/Ag_2S	20	100	0.1	99.5	140	[51]
TiO_2-doped cobalt ferrite	10	100	0.08	85	120	[52]
$Fe_{0.5}Mn_{0.5}Co_2O_4/Fe_2O_3$ composite	20	100	0.1	100	50	This study
$Mn_{0.5}Zn_{0.5}Fe_2O_4/Fe_2O_3$ nanocomposite	20	100	0.1	100	50	This study

4. Conclusions

The Pechini sol–gel technique was employed for the facile synthesis of $Mn_{0.5}Zn_{0.5}Fe_2O_4/Fe_2O_3$ and $Fe_{0.5}Mn_{0.5}Co_2O_4/Fe_2O_3$ as mixed metal oxide nanoparticles for the efficient photocatalytic degradation of Rhodamine B and Congo Red dyes. The XRD patterns revealed that the average crystallite size of the $Fe_{0.5}Mn_{0.5}Co_2O_4/Fe_2O_3$ and $Mn_{0.5}Zn_{0.5}Fe_2O_4/Fe_2O_3$ samples was 90.25 and 80.62 nm, respectively. In the presence of hydrogen peroxide, the complete degradation of 100 mL of 20 mg/L of Rhodamine B and Congo Red dyes occurred at pH = 8 and 3, respectively, within 50 min and using 0.1 g of the synthesized samples.

Author Contributions: Conceptualization, E.A.A.; methodology, E.A.A.; validation, E.A.A. and E.S.A.-F.; formal analysis, E.A.A.; resources, E.A.A.; data curation, E.S.A.-F.; writing—original draft preparation, E.S.A.-F.; writing—review and editing, E.A.A. and E.S.A.-F.; visualization, E.S.A.-F. All authors have read and agreed to the published version of the manuscript.

Funding: This research received no external funding.

Data Availability Statement: Not applicable.

Conflicts of Interest: The authors declare no conflict of interest.

References

1. Aly, H.M.; Moustafa, M.E.; Nassar, M.Y.; Abdelrahman, E.A. Synthesis and Characterization of Novel Cu (II) Complexes with 3-Substituted-4-Amino-5-Mercapto-1,2,4-Triazole Schiff Bases: A New Route to CuO Nanoparticles. *J. Mol. Struct.* **2015**, *1086*, 223–231. [CrossRef]
2. Nassar, M.Y.; Aly, H.M.; Abdelrahman, E.A.; Moustafa, M.E. Synthesis, Characterization, and Biological Activity of Some Novel Schiff Bases and Their Co(II) and Ni(II) Complexes: A New Route for Co_3O_4 and NiO Nanoparticles for Photocatalytic Degradation of Methylene Blue Dye. *J. Mol. Struct.* **2017**, *1143*, 462–471. [CrossRef]
3. Nassar, M.Y.; Aly, H.M.; Moustafa, M.E.; Abdelrahman, E.A. Synthesis, Characterization and Biological Activity of New 3-Substitued-4-Amino-5-Hydrazino-1,2,4-Triazole Schiff Bases and Their Cu(II) Complexes: A New Approach to CuO Nanoparticles for Photocatalytic Degradation of Methylene Blue Dye. *J. Inorg. Organomet. Polym. Mater.* **2017**, *27*, 1220–1233. [CrossRef]
4. Nataraj, S.K.; Hosamani, K.M.; Aminabhavi, T.M. Nanofiltration and Reverse Osmosis Thin Film Composite Membrane Module for the Removal of Dye and Salts from the Simulated Mixtures. *Desalination* **2009**, *249*, 12–17. [CrossRef]
5. Al-Bastaki, N. Removal of Methyl Orange Dye and Na2so4 Salt from Synthetic Waste Water Using Reverse Osmosis. *Chem. Eng. Process. Process Intensif.* **2004**, *43*, 1561–1567. [CrossRef]
6. Ihaddaden, S.; Aberkane, D.; Boukerroui, A.; Robert, D. Removal of Methylene Blue (Basic Dye) by Coagulation-Flocculation with Biomaterials (Bentonite and Opuntia Ficus Indica). *J. Water Process Eng.* **2022**, *49*, 102952. [CrossRef]
7. Mcyotto, F.; Wei, Q.; Macharia, D.K.; Huang, M.; Shen, C.; Chow, C.W.K. Effect of Dye Structure on Color Removal Efficiency by Coagulation. *Chem. Eng. J.* **2021**, *405*, 126674. [CrossRef]
8. Abdelrahman, E.A. Synthesis of Zeolite Nanostructures from Waste Aluminum Cans for Efficient Removal of Malachite Green Dye from Aqueous Media. *J. Mol. Liq.* **2018**, *253*, 72–82. [CrossRef]
9. Nassar, M.Y.; Abdelrahman, E.A. Hydrothermal Tuning of the Morphology and Crystallite Size of Zeolite Nanostructures for Simultaneous Adsorption and Photocatalytic Degradation of Methylene Blue Dye. *J. Mol. Liq.* **2017**, *242*, 364–374. [CrossRef]
10. Abdelrahman, E.A.; Hegazey, R.M.; Kotp, Y.H.; Alharbi, A. Spectrochimica Acta Part A: Molecular and Biomolecular Spectroscopy Facile Synthesis of Fe_2O_3 Nanoparticles from Egyptian Insecticide Cans for Ef Fi Cient Photocatalytic Degradation of Methylene Blue and Crystal Violet Dyes. *Spectrochim. Acta Part A Mol. Biomol. Spectrosc.* **2019**, *222*, 117195. [CrossRef]
11. Nassar, M.Y.; Abdelrahman, E.A.; Aly, A.A.; Mohamed, T.Y. A Facile Synthesis of Mordenite Zeolite Nanostructures for Efficient Bleaching of Crude Soybean Oil and Removal of Methylene Blue Dye from Aqueous Media. *J. Mol. Liq.* **2017**, *248*, 302–313. [CrossRef]
12. Abdelrahman, E.A.; Hegazey, R.M. Facile Synthesis of HgO Nanoparticles Using Hydrothermal Method for Efficient Photocatalytic Degradation of Crystal Violet Dye Under UV and Sunlight Irradiation. *J. Inorg. Organomet. Polym. Mater.* **2019**, *29*, 346–358. [CrossRef]
13. Alharbi, A.; Abdelrahman, E.A. Spectrochimica Acta Part A: Molecular and Biomolecular Spectroscopy Ef Fi Cient Photocatalytic Degradation of Malachite Green Dye Using Facilely Synthesized Hematite Nanoparticles from Egyptian Insecticide Cans. *Spectrochim. Acta Part A Mol. Biomol. Spectrosc.* **2020**, *226*, 117612. [CrossRef] [PubMed]
14. Hegazey, R.M.; Abdelrahman, E.A.; Kotp, Y.H.; Hameed, A.M.; Subaihi, A. Facile Fabrication of Hematite Nanoparticles from Egyptian Insecticide Cans for Efficient Photocatalytic Degradation of Rhodamine B Dye. *J. Mater. Res. Technol.* **2020**, *9*, 1652–1661. [CrossRef]
15. Abdelghany, M.M.; Ahmed, I.S.; Dessouki, H.A.; Abdelrahman, E.A. Facile Synthesis of CuO and Ag Nanoparticles by Thermal Decomposition of Novel Schiff Base Complexes. *J. Inorg. Organomet. Polym. Mater.* **2021**, *31*, 4281–4299. [CrossRef]

16. Niu, R.; Ding, Y.; Hao, L.; Ren, J.; Gong, J.; Qu, J. Plant-Mimetic Vertical-Channel Hydrogels for Synergistic Water Purification and Interfacial Water Evaporation. *ACS Appl. Mater. Interfaces* **2022**, *14*, 45533–45544. [CrossRef]
17. He, P.; Bai, H.; Fan, Z.; Hao, L.; Liu, N.; Chen, B.; Niu, R.; Gong, J. Controllable Synthesis of N/Co-Doped Carbon from Metal-Organic Frameworks for Integrated Solar Vapor Generation and Advanced Oxidation Processes. *J. Mater. Chem. A* **2022**, *10*, 13378–13392. [CrossRef]
18. Fan, D.; Lu, Y.; Zhang, H.; Xu, H.; Lu, C.; Tang, Y.; Yang, X. Synergy of Photocatalysis and Photothermal Effect in Integrated 0D Perovskite Oxide/2D MXene Heterostructures for Simultaneous Water Purification and Solar Steam Generation. *Appl. Catal. B Environ.* **2021**, *295*, 120285. [CrossRef]
19. Abdelwahab, M.A.; El Rayes, S.M.; Kamel, M.M.; Abdelrahman, E.A. Encapsulation of NiS and ZnS in Analcime Nanoparticles as Novel Nanocomposites for the Effective Photocatalytic Degradation of Orange G and Methylene Blue Dyes. *Int. J. Environ. Anal. Chem.* **2022**, 1–18, *in press*. [CrossRef]
20. Almehizia, A.A.; Al-Omar, M.A.; Naglah, A.M.; Hegazey, R.M.; Al-Wasidi, A.S.; Katouah, H.A.; Basha, M.T.; Alghanmi, R.M.; Khedr, A.M.; Algethami, F.K.; et al. Facile Synthesis of Copper Carbonate/Cobalt Carbonate/Manganese Carbonate and Copper Oxide/Cobalt Manganese Oxide/Manganese Oxide as Novel Nanocomposites for Efficient Photocatalytic Degradation of Crystal Violet Dye. *Int. J. Environ. Anal. Chem.* **2022**, 1–21. [CrossRef]
21. Amalina, F.; Syukor, A.; Razak, A.; Krishnan, S.; Zularisam, A.W.; Nasrullah, M. A Review of Eco-Sustainable Techniques for the Removal of Rhodamine B Dye Utilizing Biomass Residue Adsorbents. *Phys. Chem. Earth* **2022**, *128*, 103267. [CrossRef]
22. Srivind, J.; Nagarethinam, V.S.; Suganya, M.; Balamurugan, S.; Prabha, D.; Balu, A.R. Visible Light Irradiated Photocatalytic Performance of SnS2-CdO Nanocomposite against the Degradation of Rhodamine B (Cationic) and Congo Red (Anionic) Dyes. *Mater. Sci. Eng. B Solid-State Mater. Adv. Technol.* **2020**, *255*, 114530. [CrossRef]
23. Oladoye, P.O.; Bamigboye, M.O.; Ogunbiyi, O.D.; Akano, M.T. Toxicity and Decontamination Strategies of Congo Red Dye. *Groundw. Sustain. Dev.* **2022**, *19*, 100844. [CrossRef]
24. In, S.-I.; Berg, R. Visible Light Induced Degradation of Methylene Blue on Titanium Oxo Ethoxo Clusters of Type $Ti_{16}O_{16}$(OEt)32. *Asian J. Chem.* **2012**, *24*, 428–432.
25. In, S.; Vesborg, P.C.K.; Abrams, B.L.; Hou, Y.; Chorkendorff, I. A Comparative Study of Two Techniques for Determining Photocatalytic Activity of Nitrogen Doped TiO_2 Nanotubes under Visible Light Irradiation: Photocatalytic Reduction of Dye and Photocatalytic O. *J. Photochem. Photobiol. A Chem.* **2011**, *222*, 258–262. [CrossRef]
26. Shammi, Z.M.; Kianfar, A.; Momeni, M.M. Photocatalytic Degradation and Mineralization of Dye Pollutants from Wastewater under Visible Light Using Synthetic CuO-VO_2/TiO_2 Nanotubes/Nanosheets. *J. Mater. Sci. Mater. Electron.* **2021**, *32*, 20149–20163. [CrossRef]
27. Castro, L.V.; Ortíz-Islas, E.; Manríquez, M.E.; Albiter, E.; Cabrera-Sierra, R.; Alvarado-Zavala, B. Photocatalytic Degradation of Mixed Dyes in Aqueous Phase by MgAlTi and ZnAlTi Mixed Oxides. *Top. Catal.* **2021**, *64*, 97–111. [CrossRef]
28. Nasr, R.A.; Abbas, H.A.; Vannier, R.N.; Jamil, T.S. Preparation, Characterization and Photocatalytic Decolorization Process for the Removal of Orange-Green Dye Using Perovskites Ba1-XBixFeO_3-δ (x = 0, 0.05, 0.1). *Inorg. Nano-Metal Chem.* **2022**, *52*, 1123–1133. [CrossRef]
29. Sodeinde, K.O.; Olusanya, S.O.; Enogheghase, V.F.; Lawal, O.S. Photocatalytic Degradation of Janus Green Blue Dye in Wastewater by Green Synthesised Reduced Graphene Oxide-Silver Nanocomposite. *Int. J. Environ. Anal. Chem.* **2022**, 1–17. [CrossRef]
30. Patil, S.P.; Shrivastava, V.S.; Sonawane, G.H. Photocatalytic Degradation of Rhodamine 6G Using ZnO-Montmorillonite Nanocomposite: A Kinetic Approach. *Desalination Water Treat.* **2015**, *54*, 374–381. [CrossRef]
31. Mahadwad, O.K.; Parikh, P.A.; Jasra, R.V.; Patil, C. Photocatalytic Degradation of Reactive Black-5 Dye Using TiO_2-Impregnated Activated Carbon. *Environ. Technol.* **2012**, *33*, 307–312. [CrossRef] [PubMed]
32. Amoli, A.E.; Masoumi, M.; Sharifzadeh, M.; Babaei, F.; Firouzzade Pasha, G. Synthesis of TiO_2-Fe_2O_3 Nanocomposite for the Photocatalytic Degradation of Direct Blue 199 and Basic Yellow 28 Dyes under Visible Light Irradiation. *J. Dispers. Sci. Technol.* **2021**, 1–9. [CrossRef]
33. Salavati-Niasari, M.; Soofivand, F.; Sobhani-Nasab, A.; Shakouri-Arani, M.; Hamadanian, M.; Bagheri, S. Facile Synthesis and Characterization of $CdTiO_3$ Nanoparticles by Pechini Sol–Gel Method. *J. Mater. Sci. Mater. Electron.* **2017**, *28*, 14965–14973. [CrossRef]
34. Hajizadeh-Oghaz, M.; Razavi, R.S.; Barekat, M.; Naderi, M.; Malekzadeh, S.; Rezazadeh, M. Synthesis and Characterization of Y2O_3 Nanoparticles by Sol–Gel Process for Transparent Ceramics Applications. *J. Sol-Gel Sci. Technol.* **2016**, *78*, 682–691. [CrossRef]
35. Potůček, Z.; Trepakov, V.A.; Makarova, M.V.; Sazama, P.; Badalyan, A.G.; Dejneka, A.; Jastrabik, L. Luminescent Impurity Ion Probe and Low Temperature Phase of $SrTiO_3$ Nanoparticles. *Mater. Sci. Technol.* **2009**, *25*, 1334–1340. [CrossRef]
36. Wu, Y.T.; Wang, X.F.; Yu, C.L.; Li, E.Y. Preparation and Characterization of Barium Titanate ($BaTiO_3$) Nano-Powders by Pechini Sol-Gel Method. *Mater. Manuf. Process.* **2012**, *27*, 1329–1333. [CrossRef]
37. Abdelrahman, E.A.; Hegazey, R.M. Utilization of Waste Aluminum Cans in the Fabrication of Hydroxysodalite Nanoparticles and Their Chitosan Biopolymer Composites for the Removal of Ni(II) and Pb(II) Ions from Aqueous Solutions: Kinetic, Equilibrium, and Reusability Studies. *Microchem. J.* **2019**, *145*, 18–25. [CrossRef]

38. Abdelrahman, E.A.; Hegazey, R.M. Exploitation of Egyptian Insecticide Cans in the Fabrication of Si/Fe Nanostructures and Their Chitosan Polymer Composites for the Removal of Ni(II), Cu(II), and Zn(II) Ions from Aqueous Solutions. *Compos. Part B Eng.* **2019**, *166*, 382–400. [CrossRef]
39. Abdelrahman, E.A.; Abou El-Reash, Y.G.; Youssef, H.M.; Kotp, Y.H.; Hegazey, R.M. Utilization of Rice Husk and Waste Aluminum Cans for the Synthesis of Some Nanosized Zeolite, Zeolite/Zeolite, and Geopolymer/Zeolite Products for the Efficient Removal of Co(II), Cu(II), and Zn(II) Ions from Aqueous Media. *J. Hazard. Mater.* **2021**, *401*, 123813. [CrossRef]
40. Krishnan, S.G.; Harilal, M.; Arshid, N.; Jagadish, P.; Khalid, M.; Li, L.P. Rapid Microwave-Assisted Synthesis of $MnCo_2O_4$ Nanoflakes as a Cathode for Battery-Supercapacitor Hybrid. *J. Energy Storage* **2021**, *44*, 103566. [CrossRef]
41. Chakraborty, M.; Bera, K.K.; Chatterjee, S.; Ghosh, A.; Bhattacharya, S.K. Synthesis of Mesoporous BiOI Flower and Facile In-Situ Preparation of BiOI/BiOCl Mixture for Enhanced Photocatalytic Degradation of Toxic Dye, Rhodamine-B. *J. Photochem. Photobiol.* **2021**, *8*, 100077. [CrossRef]
42. Hamza, M.A.; Abd El-Rahman, S.A.; Abou-Gamra, Z.M. Facile One-Pot Solid-State Fabrication of a Novel Binary Nanocomposite of Commercial ZnO and Commercial $PbCrO_4$ with Enhanced Photocatalytic Degradation of Rhodamine B Dye. *Opt. Mater.* **2022**, *124*, 111987. [CrossRef]
43. Maruthupandy, M.; Muneeswaran, T.; Chackaravarthi, G.; Vennila, T.; Anand, M.; Cho, W.S.; Quero, F. Synthesis of Chitosan/SnO_2 Nanocomposites by Chemical Precipitation for Enhanced Visible Light Photocatalytic Degradation Efficiency of Congo Red and Rhodamine-B Dye Molecules. *J. Photochem. Photobiol. A Chem.* **2022**, *430*, 113972. [CrossRef]
44. Bilgic, A. Fabrication of MonoBODIPY-Functionalized Fe_3O_4@SiO_2@TiO_2 Nanoparticles for the Photocatalytic Degradation of Rhodamine B under UV Irradiation and the Detection and Removal of Cu(II) Ions in Aqueous Solutions. *J. Alloys Compd.* **2022**, *899*, 163360. [CrossRef]
45. Rafieezadeh, M.; Kianfar, A.H. Fabrication of Heterojunction Ternary $Fe_3O_4/TiO_2/CoMoO_4$ as a Magnetic Photocatalyst for Organic Dyes Degradation under Sunlight Irradiation. *J. Photochem. Photobiol. A Chem.* **2022**, *423*, 113596. [CrossRef]
46. Madima, N.; Kefeni, K.K.; Mishra, S.B.; Mishra, A.K.; Kuvarega, A.T. Fabrication of Magnetic Recoverable Fe_3O_4/TiO_2 Heterostructure for Photocatalytic Degradation of Rhodamine B Dye. *Inorg. Chem. Commun.* **2022**, *145*, 109966. [CrossRef]
47. Jansanthea, P.; Kanthabangharn, J.; Chomkitichai, W.; Ketwaraporn, J. Temperature-Controlled Synthesis and Photocatalytic Properties of ZnO-SnO_2 Nanocomposites. *J. Aust. Ceram. Soc.* **2021**, *57*, 579–588. [CrossRef]
48. Davis, M.; Hung-Low, F.; Hikal, W.M.; Hope-Weeks, L.J. Enhanced Photocatalytic Performance of Fe-Doped SnO_2 Nanoarchitectures under UV Irradiation: Synthesis and Activity. *J. Mater. Sci.* **2013**, *48*, 6404–6409. [CrossRef]
49. Hokonya, N.; Mahamadi, C.; Mukaratirwa-Muchanyereyi, N.; Gutu, T.; Zvinowanda, C. Green Synthesis of $P - ZrO_2CeO_2ZnO$ Nanoparticles Using Leaf Extracts of Flacourtia Indica and Their Application for the Photocatalytic Degradation of a Model Toxic Dye, Congo Red. *Heliyon* **2022**, *8*, e10277. [CrossRef]
50. Güy, N.; Özacar, M. The Influence of Noble Metals on Photocatalytic Activity of ZnO for Congo Red Degradation. *Int. J. Hydrogen Energy* **2016**, *41*, 20100–20112. [CrossRef]
51. Jabbar, Z.H.; Graimed, B.H.; Issa, M.A.; Ammar, S.H.; Ebrahim, S.E.; Khadim, H.J.; Okab, A.A. Photocatalytic Degradation of Congo Red Dye Using Magnetic Silica-Coated Ag_2WO_4/Ag_2S as Type I Heterojunction Photocatalyst: Stability and Mechanisms Studies. *Mater. Sci. Semicond. Process.* **2023**, *153*, 107151. [CrossRef]
52. Magdalane, C.M.; Priyadharsini, G.M.A.; Kaviyarasu, K.; Jothi, A.I.; Simiyon, G.G. Synthesis and Characterization of TiO_2 Doped Cobalt Ferrite Nanoparticles via Microwave Method: Investigation of Photocatalytic Performance of Congo Red Degradation Dye. *Surf. Interfaces* **2021**, *25*, 101296. [CrossRef]
53. Feng, K.; Zhang, L.; Gong, J.; Qu, J.; Niu, R. Visible Light Triggered Exfoliation of COF Micro/Nanomotors for Efficient Photocatalysis. *Green Energy Environ.* 2021; *in press*. [CrossRef]
54. Maggard, P.A. Capturing Metastable Oxide Semiconductors for Applications in Solar Energy Conversion. *Acc. Chem. Res.* **2021**, *54*, 3160–3171. [CrossRef] [PubMed]
55. Feng, K.; Gong, J.; Qu, J.; Niu, R. Dual-Mode-Driven Micromotor Based on Foam-like Carbon Nitride and Fe_3O_4 with Improved Manipulation and Photocatalytic Performance. *ACS Appl. Mater. Interfaces* **2022**. [CrossRef]
56. Li, J.; Li, J.; Wu, C.; Li, Z.; Cai, L.; Tang, H.; Zhou, Z.; Wang, G.; Wang, J.; Zhao, L.; et al. Crystalline Carbon Nitride Anchored on MXene as an Ordered Schottky Heterojunction Photocatalyst for Enhanced Visible-Light Hydrogen Evolution. *Carbon.* **2021**, *179*, 387–399. [CrossRef]